Mémoire

Auteur : Chawla, Arjun
Promoteur(s) : Sluse, Dominique
Faculté : Faculté des Sciences
Diplôme : Master en sciences spatiales, à finalité approfondie
Année académique : 2021-2022
URI/URL : http://hdl.handle.net/2268.2/15361

Department of Astrophysics, Geophysics and Oceanography
Faculty of Sciences
University of Liège

Deciphering a gravitationally lensed system with the ESO-MUSE integral field spectrograph

Arjun Chawla

A thesis presented for the degree of
Master of Science

Supervisor:
Dominique Sluse

Reading Committee:
Gilles Orban de Xivry
Đorđe Savić
Ludovic Delchambre

15th August 2022

Academic year 2021-2022

Contents

Acknowledgements

Firstly, i would like to thank my supervisor Dominique Sluse for his guidance, patience and virtue to help me learn and grow through this work.

I thank G.Orban de Xirvy, Đ. Savić and L. Delchambre for accepting to be part of the jury for this work.

I heartily thank Lyne, Matt and Zoe regarding conversations to help shape this work and i also thank Angelo, Michelle, Guillaume, Clementine, Jakob, Pierre, Mathilde, Lorenzo and Jahanvi for their friendship and support.

Finally, i would like to thank my parents and my brother for their continuous love and support.

Goals of this master thesis

Quasars or QSOs (quasi stellar objects) are extremely bright objects and a subclass of AGNs (active galactic nucleus). AGNs are objects which have non-stellar activity in their nucleus. This activity is due to accretion around the black hole (BH) in the nucleus. An AGN is characterized by broad emission lines. It is called a quasar when its absolute magnitude in the V band is $<$ -23[1]. The BH in the nucleus can generally be a supermassive black hole and its mass can be as large as $10^8 M\odot$ (solar masses)[13].

The equivalence principle, which is the equivalence of gravitational and inertial mass, acts as the foundation for the general relativity theory by Einstein. Einstein, demonstrated through it that gravitational fields have to bend light [11]. If a massive object is present between us and a source of electromagnetic radiation, it can thus deflect light resulting in multiple images of the source, which would be separated by small angles and is the principle of gravitational lensing. This was predicted in [10], and Einstein [12] studied this effect for a star on another star, but concluded that the images would be split by too small a scale to be detected. Image separation produced by a lens depends on $\sqrt{mass}$ of the lens and thus, a galaxy or a rich galaxy cluster is a better candidate for a lens [7] provided a distant and bright enough source is present to be able to visualize this phenomenon. A supernova as a source was originally thought to be a good candidate to study gravitational lensing, but in practice, luminous quasars are found to be the best candidate with numerous observational evidences.

Integral Field Spectroscopy (IFS) with adaptive optics provides an ideal tool to dissect such a lensed system and study it and this is explained in more detail in section 1. For the purpose of this work, the system 2M1134-2103 which is being monitored for cosmography studies (further details in section 4) is studied in detail with the help of ESO MUSE spectrograph.

Several information can be derived for such a system with an instrument like MUSE, which include measuring the lens/source redshift, study its environment (as objects in the FOV can produce extra light deflection), study the emissions and absorptions in the spectrum of the lens, and the source to derive properties of the system.

At the beginning of this thesis, the lens redshift was unknown and thus one of the primary goals of this work was to extract the spectrum for the lens (done in section 3) and find its redshift (section 3.1.1).

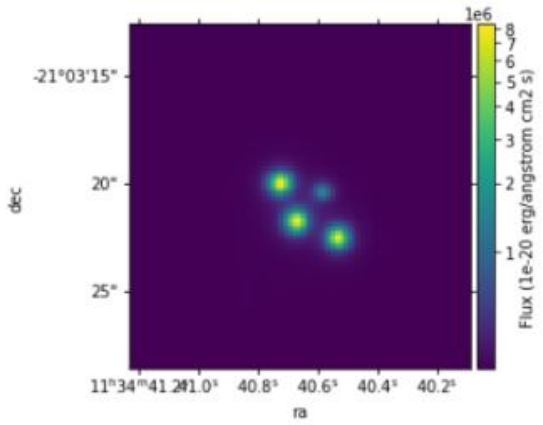

Figure 1: White light image for the gravitationally lensed quasar system 2M1134+2103 based on MUSE data

The extracted spectrum of both the lens and the quasar contains various information that can be analysed besides the redshift. The emissions and absorptions in the lens and source spectrum can give information about the nature of the lensing galaxy and the quasar. Absorption lines in quasars can also provide information about the intervening objects in the FOV producing those absorptions (section 3.2.2).

For the system 2M1134+2103, we have a quadruple imaged quasar (fig 1), and some compact sources in the lens like a star or a planet, can produce a smaller amplitude gravitational light deflection in one or more images of the quasar. This effect is called microlensing and is discussed more in detail in section 5. The goal is to search for spectral deformation of the quasar spectrum caused by microlensing. Such deformation can be used to probe the structure of the quasar. In that context, it is also important to characterise the physical properties of the quasar in order to infer the size of the emitting region. In particular, the BH mass can be derived based on the width of the broad emission lines and luminosity at the continuum. This is discussed in detail in section 4.

But before we get all this information from the science data, the raw data received from MUSE is converted into usable science data through a data reduction process. To obtain the best possible science data for this work, the data reduction process is first described and then optimized and is thus discussed in detail in section 2.

1 MUSE Instrument

The MUSE Instrument (Multi Unit Spectroscopic Explorer) is an instrument mounted on the Nasmyth focus at the VLT (Very Large Telescope) of ESO (European Southern Observatory). It is an Integral-field spectrograph operating in the visible wavelength ranges of 480-930nm with a resolving power of R=3000.

It splits the adaptive optics corrected field of view into 24 sub-fields (channels) and each of these sub-fields is fed into a spectrograph called Integral field unit or IFU. An image slicer in front of the IFU serves to be an entrance slit, further splitting the incoming light into 48 slices. (An example of this can be show with a raw data image for a random channel shown in fig 2). Hence, the slit is optically cut into smaller pieces and the data is re-imaged on the image plane at several locations. This provides an advantage that a spectrum can be obtained for a large field of view.

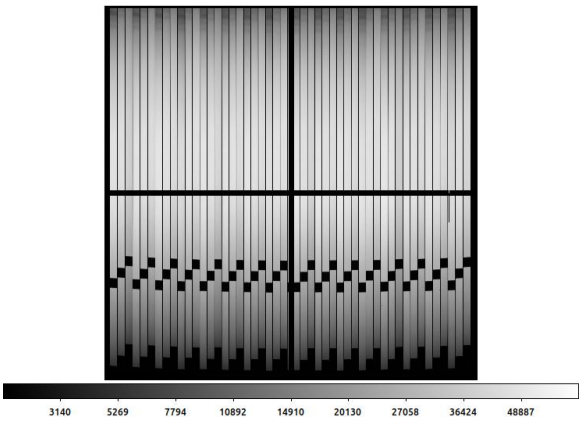

Figure 2: Raw data image for channel 23

MUSE uses adaptive optics through its adaptive optics system called GALACSI to correct for atmospheric turbulence. GALACSI provides 2 instrument modes, the WFM (wide field mode) and NFM (narrow field mode). Both modes use a natural guide star and a LGS (Laser guide stars), but their nature and location differ in each mode. For the observation of gravitationally lensed quasar images the WFM is used to study the objects in the FOV of the quasar. In the WFM, MUSE covers 1' by 1' FOV with sampling of 0.2" per spatial pixel. GALACSI makes use of 4 Sodium LGS launched from the VLT and the light emitted by those, at an altitude of 80-100km in the earth's atmosphere is collected by 4 different wave front sensors. They are then combined by a computer in real time to find the approximation of the wave front error

which is then corrected for the data. One visible guide star <17.5 R-mag is then used to correct for the remaining atmospheric tip-tilt, which is correcting the tilts of the wave fronts.

MUSE also uses two filters which can be optionally inserted along the light-path. Firstly, it uses a notch filter to suppress the wavelength of the NaD line at 589nm and the second filter cuts off light in the blue part at wavelength ranges 465-480nm. These filters are used so the atmospheric correction performed with the help of the LGS and the natural guide star do not contaminate the data at these wavelengths.

1.1 Observations

23 exposures of 600 seconds each were taken for 2M1134-2103 between 13/03/2021-16/04/2021. The observing sequence was designed to have 4 consecutive exposures placing the objects in a different quadrant as shown in fig 3. This sequence of exposures taken in a row is called an observing block. The advantage of using this method of taking observations is that it covers a larger FOV when the combination of the images is done which could be useful to study the objects in the FOV of the quasar as well as to mitigate biases introduced by any defects or systematics in a part of the detector. Combining over all the exposures this way would average out those defects. The observation log is displayed in table 1.

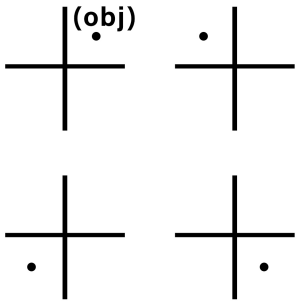

Figure 3: Orientation of the object in MUSE FOV

S.No	Date	Exptime	RA	DEC	Seeing	Airmass
1	13/03/2021	600	173.664668	-21.05228	0.51	1.658
2	13/03/2021	600	173.664688	-21.05228	0.54	1.562
3	13/03/2021	600	173.673362	-21.06017	0.60	1.479
4	13/03/2021	600	173.673151	-21.05228	0.49	1.407
5	14/03/2021	600	173.665561	-21.05331	0.62	1.749
6	14/03/2021	600	173.665771	-21.06100	0.54	1.636
7	14/03/2021	600	173.674255	-21.06100	0.62	1.540
8	14/03/2021	600	173.674044	-21.05311	0.58	1.456
9	07/04/2021	600	173.665055	-21.05161	1.09	1.365
10	07/04/2021	600	173.665265	-21.05950	0.94	1.306
11	15/04/2021	600	173.664260	-21.05280	0.77	1.226
12	15/04/2021	600	173.664470	-21.06069	0.87	1.187
13	15/04/2021	600	173.672953	-21.06069	0.75	1.153
14	15/04/2021	600	173.672473	-21.05280	0.62	1.124
15	16/04/2021	600	173.665561	-21.05145	0.62	1.272
16	16/04/2021	600	173.665771	-21.05933	0.90	1.226
17	16/04/2021	600	173.674254	-21.05933	0.79	1.187
18	16/04/2021	600	173.674044	-21.05144	1.14	1.151
19	16/04/2021	600	173.665771	-21.05933	0.72	1.118
20	16/04/2021	600	173.664371	-21.05172	0.72	1.076
21	16/04/2021	600	173.664581	-21.05961	0.86	1.057
22	16/04/2021	600	173.673064	-21.05961	0.64	1.041
23	16/04/2021	600	173.673270	-21.05172	0.76	1.028

Table 1: Observation log

2 Reduction and combination

The raw data obtained from the observations needs to be reduced and calibrated before it can be used for scientific purposes. The data obtained from the MUSE instrument is reduced and calibrated with the help of the designed MUSE pipeline. The pipeline is run within a GUI interface called esoreflex which calls command-line scripts called esorex. The software, esoreflex uses the esorex for each reduction step in the pipeline [15]. In the following subsections i explain how the pipeline is handling the data and the necessary steps it is performing.

The pipeline handles the data in two big steps. Firstly, it performs basic science reduction which include seven calibration recipes and a pre-processing recipe which work firstly to remove the signature of each individual IFU. Then this pre-processing data is used in the next big step where another 3 calibrations are performed and the final reduced data is obtained which can now be used for science.

The reason the data reduction process is important to explain here is because during the course of work, several checks were performed to see if the pipeline was working correctly for the data used in this thesis which are explained in the sections below. Most of the data reduction process was understood with the help of [48] and the recipes with the help of [46].

2.1 Basic science reduction

For the basic science reduction we correct for the dark, the bias and the flat field. Then perform a wavelength calibration and estimate the lsf (line spread function), geometry and twilight and then finally we use the pre-processing recipe, *muse_scibasic*.

2.1.1 Bias

For each pixel in the CCD the voltage can be converted to a positive number. For an ideal CCD, the bias would be the same for every pixel and unvarying over time, but in reality it can be minutely different for each pixel during a night or from one night to another. So, usually to account for the bias, bias images are taken with a closed shutter and zero exposure time and the frames are recorded and immediately read out from the CCD. MUSE takes 11 of these images every night and since the MUSE CCD are read out in four quadrants, the bias already shows four different values in

the middle of the read-out image. The bias has to be subtracted as a 2D image from the science data as they show horizontal and vertical gradients on top of the quadrant pattern.

Overscan regions are generated when the CCD continues to read beyond the pixels that are physically available. In MUSE, they are located in a cross pattern inside, between the quadrants of the CCD. These regions play an important role as the gradients are changing over time, and these regions can be analyzed to correct for the bias. Due to cosmic rays or hot columns or pixels whose readout value spills into the overscan region, values that strongly deviate can appear in the analysis of the overscan region and so these should be accounted for. The method, MUSE uses to deal with it is by modelling the slope of the vertical overscan with a polynomial. Using these values from the overscan can determine the offset to the actual bias determined for the other exposure and so this offset can be applied to account for the variation of the bias level with time.

The workflow itself keeps track of the noise at each step of the reduction. The RON (Read-out noise) associated to each CCD and uncertainty estimates are important to calculate the variance associated to the data, and bias images are used to obtain the RON.

The recipe *muse_bias* in the pipeline with the default option vpoly for the overscan correction as describe above is used to create a master bias file that is then used in the next reductions steps. The masterbias file created by this recipe for a random exposure and channel is shown here in fig 4.

2.1.2 Dark

When no outside radiation or photons are entering the CCD, there can still be charges generated and due to these charges there is a minuscule amount of electric current in the CCD called the dark current. Potentially important, its a source for instrumental noise and is found to be very small with the MUSE detectors (typically of the order of 1 e^-/h/pixel). These dark currents have a pattern noise. The pattern for this noise can be estimated by constructing dark frames and remove it from the data.

A smooth model of the dark can also be created with the pipeline. Here, from the science exposures, the dark current can be subtracted at a pixel level to avoid adding

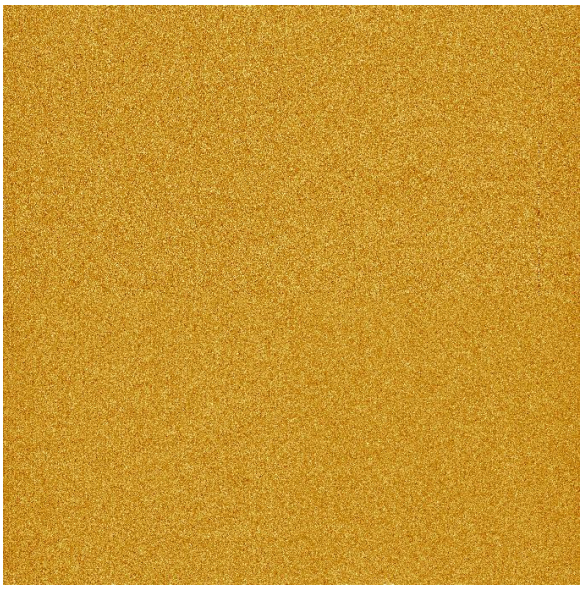

Figure 4: Master bias for channel 3 in exposure 20 from table 1

any additional noise. This is done in 3 steps :

1. A model of fitting a 2D polynomial of 5th order over a horizontal region is created.
2. A bi-linear polynomial is fit where the edge of the CCDs are ignored to represent large scale dark currents. This is done so the uneven borders and corners which can be heated by the read-out ports of the CCD don't contribute.
3. The read-out ports are modeled separately around each of the 4 corners using a 5th order polynomial.

The sum of all these 3 models is the final dark model. Using the statistics of the difference between the master dark and this dark model are then used to locate the bad pixels in future steps. The master dark is created using the *muse_dark* recipe and may not be needed in the further processing steps as the dark current is usually very small in the MUSE CCDs.

2.1.3 Flat-Fielding

The sensitivity in pixels can vary in the CCD, due to dust on its optical surface or even variations in the illumination of its optical system there can be anomalies in

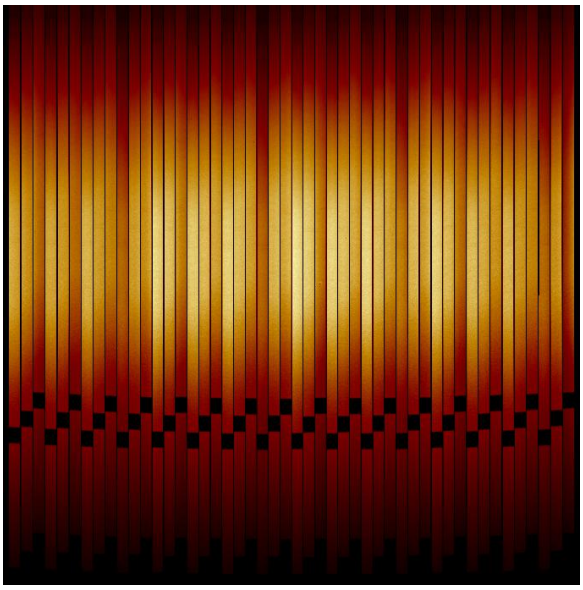

Figure 5: Masterflat for channel 8 and exposure 17 from table 1

its optical path. Flat fielding is used to correct for these anomalies by dividing the science images by the created flat fields. The flat fields are usually created by using a source to uniformly illuminate the CCD and then the anomalies are the variations that arise in the illumination.

The CCD is illuminated with continuum lamps and a series of exposures are taken. The bias is then subtracted from these exposures and the data is converted from the adu value (which is a digital count) to electrons using the gain of the CCD. The gain of the CCD is the number of electrons that are photo-excited to produce a single digital count. The flat-field images are then combined using a 3σ clipped mean and the final master flat is obtained.

Alongside the creation of the master flat, slice tracing is also performed simultaneously. For each IFU, there are 48 slices for each image. Around the center of the area of the data, an average horizontal cut is extracted. The median value of the cut is determined and pixels falling below half of this value determine a guess for the edges of each slice. The flat field for a random exposure and channel is shown in fig 5.

Once the edges of the slices are known through slice tracing, dark pixels can be found using the master flat field for each CCD row, in between the edges of every slice. The

outliers found using sigma-clipped statistics are dark pixels and these can be flagged and propagated in further steps of the calibrations.

2.1.4 Wavelength calibration

Due to environmental conditions over time, the wavelengths assigned to each pixel on the CCD can drift over time and thus regular wavelength calibrations is required to ensure accurate wavelengths for the science data.

MUSE has 3 integrated arc lamps, mainly HgCd, Ne and a Xe lamp. Using 3 different lamps ensures that the entire wavelength range required by the instrument is covered by these lamps. 5 exposures are taken from each lamp as to have a maximum S/N ratio. Five exposures ensure that the faintest lines have enough flux and the brightest ones don't oversaturate the detector. A raw arc lamp exposure is shown in fig 6. All images are then bias subtracted but usually for computing the wavelength solution, the dark and flats are not needed. The exposures are taken by each arc lamp and then combined using a 3σ clipped average. The advantage of doing this is that the emission lines are then easier to identify. The emission lines are identified separately in each slice and the line relevant to the corresponding arc lamp is chosen to be the best fit. First, a S/N spectrum is created from the middle of each slice in the CCD by diving the data with its standard deviation. A median smoothed version is subtracted to remove any constant background and the lines are fit with a Gaussian of 1σ to get the line center. For WFM, about 100-150 peaks are detected and associated with 90-120 known arc lines. The deviant lines are rejected which could appear due to hot pixels or dark columns and thus a wavelength solution is calculated using iterations of 2D polynomial fit to the center of all the measured arc lines at their reference wavelength using a 3σ clipping level. This 2D polynomial has a 'horizontal' order of 2 (which describes the curvature of the arc lines in each slice of the CCD) and a 'vertical' order of 6 (used to describe the relation between wavelength and dispersion relation) by default. The wavelength solution is calculated using the *muse_wavecal* recipe in the pipeline and its accuracy is 0.06-0.08 Å corresponding to a 1σ velocity precision of 2.5-4 km s^{-1}.

The application of this solution works well in the daytime, but in the nighttime, when the data is supposed to be taken, there is a change in the ambient temperature which causes the change of the CCD temperature. This causes a zero point shift in the

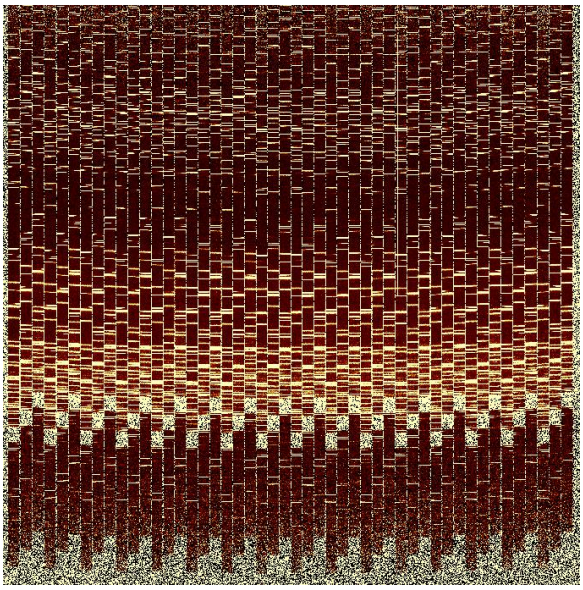

Figure 6: Arc lamp exposure

wavelengths that is not negligible. This shift is computed with the help of sky lines with the default one being the [OI] line at 5577.339 and 6300.304 Å. This line is given weight while computing the standard deviations of the lines fitted by gaussians to get the central point to correct for the zero shift. Unless there is a significant emission at these wavelengths in the science data, this line works as a good model for the zero shift correction for nighttime.

A wavelength solution calibrated arc lamp frame for the data used in this thesis is shown in fig 7.

2.1.5 Geometric Calibration

There are 24x48=1152 slices, but one needs to determine the precise positions of these slices corresponding to the FOV which is done with geometric calibration. The aim is to measure on the FOV, the x and y positions corresponding to each slice, their width and their angle. This is done with the help of a pinhole mask containing a specific number of holes spread out across different rows. The gaps in the mask are in such a way that three pinholes are simultaneously illuminated in a particular slice in the image slicer. The mask is vertically moved across the FOV and the arc lamps are used as an illumination source. If a pinhole is illuminated it corresponds to a specific location in the CCD. The instrumental properties to determine the expected position

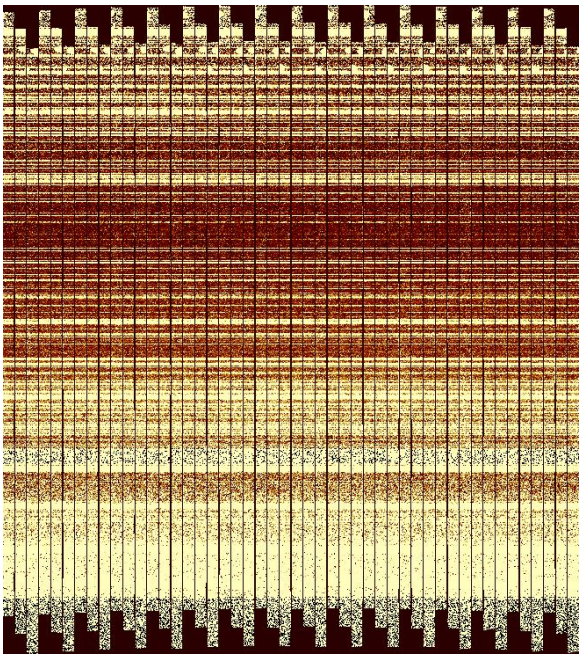

Figure 7: Wavelength solution calibrated arc lamp frame

of these bright spots illuminated by the holes in the mask is determined from the slice tracing done in the flat fielding process (the trace table) and the wavelength calibration table with the layout of the mask.

The trace table, wavelength calibration table and the line catalog are used to detect the spots of the arc lines. Thirteen of the brightest lines are isolated and a rectangular window is constructed for each slice and the arc line over the full width of the slice on the CCD. In this window, the source is detected with the help of a threshold which is equal to 2.2σ of absolute median deviation of these bright lines. Exactly 3 spots should be detected in each slice corresponding to the holes of the mask, and if we have more than 3 it means there are some artifacts that are detected. The flux in all the spots is measured along with the centroid and FWHM by fitting a 2D Gaussian. This way we obtain the result for each of the 3 spots, in each slice, for each arc line and each exposure to get the spatial positions in the CCD as well as the flux. This models well the vertical distance of the pinholes but the motion of the mask is not well calibrated yet so we obtain uncertainties on the angle of the mask inside the mask wheel and its relative motion. The effective pinhole distance is self calibrated with the help of actual data.

The slice position in the FOV is taken as a weighted average for each fitted arc line in each slice and the weighted error estimates computing the standard deviations help to accurately determine the precise positions of the slices in the FOV and is all done with the help of the *muse_geometry* recipe in the pipeline.

2.1.6 Twilight sky flat

Illumination of the objects in the sky is nearly emulated but not perfectly by the illumination of the detector by the flat-field [25]. Flat-fielding gets rid of the pixel to pixel variation but twilight flats are needed for uniform illumination. Thus, For this purpose, a series of sequences is started before sunset to take bright sky background exposures (the sky provides uniform illumination) as to reach high illuminations in short exposures to simulate the conditions of the MUSE instrument with a constant background and then to remove the residual gradients.

The skyflat images are then bias subtracted, flat fielded, converted from adu to e^- and combined using 3σ clipped average. In these combined images, every pixel is assigned a 3D coordinate creating a pixel table for each IFU, which are used to create a data cube. Since the AO method is used, pixels associated to the wavelengths near the effect of the NaD laser contain only noise due to the use of notch filter so as to not contaminate the data in this wavelength range (with the flux of the laser guide stars) and is removed from the pixel table and the constructed data cube. A white light image is created from this cube and so the pixel table, the data cube and the white light images are saved at this stage.

2.1.7 Line spread function

The line spread function, is a function that gives information on the line shape as a function of wavelength in response to a monochromatic light source and is thus important to measure for a good sky subtraction. For this purpose, the wavelength calibration and its solution calculated is used. The LSF is better measured if long exposures are used for each of the arc lamps to get a better S/N ratio. These raw exposures are bias subtracted, corrected for the overscan and divided by the flat field. To represent the line shape as a function of the wavelength, either a 2D interpolated image for each slice and IFU, generated by the pipeline can be used or a Gauss-Hermite function that tracks the coefficients in a tabular structure can also be used.

The pipeline provides both these options but using the Gauss-Hermite function is computationally more expensive, so in the data used in the thesis and in general the previous option is used. This is done through the recipe *muse_lsf* in the pipeline.

2.1.8 scibasic

The *muse_scibasic* recipe is used to remove all the instrumental signatures that could affect the data. It processes individually, each of the 24 channels. The raw CCD image is read in a DATA extension and two new images are added called DQ for data quality and STAT for variances in the data, which are initially empty. The bad pixel table created in the earlier stages of the calibration from the hot pixels and the dark pixels are marked in the DQ image and additionally the saturated pixels are marked as bad pixels as well. The overscan regions are then analyzed before the master bias created in the bias step is subtracted. The CCD gain is then used to change units from adu to e^- and then the master dark is subtracted. The image is then divided by the flat field.

The trace table, wavelength calibration table and the geometry table are then used to create a cube of spatial and wavelength axis and each CCD-based pixel is assigned the corrected data value and hence a pixel table is created for each input science exposure.

The wavelength zero point correction is done if applicable using the sky emission lines and then the pixel table is cropped to a value corresponding to which the FOV is fully sampled. For the data reduced during this thesis, that range corresponds to values between 4700-9350 Å. The last processing step injects the twilight sky cube to the corresponding value of each pixel in the pixel table where the data values are divided by the twilight sky cube. Thus, at the end of this stage, a pre-reduced pixel table for each channel is obtained.

2.2 Post Processing

The result of this process is to obtain a final reduced data cube, a pixel table and a white light image for an exposure.

2.2.1 Raman scattering correction

Due to the usage of laser guide stars in AO, new emission lines of telluric origin around 0_2 were discovered in the spectra which arise due to Raman scattering of the laser guide star. They appear at around 6484 and 6827 Å as bright peaks and extending as secondary peaks to a range of 50 Å from the main peaks. Thus, these lines can be detected, modeled and removed from the data in the final post processing step as an option.

2.2.2 Autocal

When data is integrated over several wavelengths to construct an image from the data cube, a pattern is left within each IFU and even at the level of single slices, where pixels could have a slight difference in illuminations with the neighbouring pixels, so the pipeline provides a feature for autocalibration on the slice level in deep field surveys for object detection where much of the sky background is blank. This is done by setting autocal=deepfield or autocal=user in the *muse_scipost* recipe.

2.2.3 Atmospheric refraction correction

This is an important step for ground based observations. There can be a significant shift with wavelength, of the position of an object within a data cube which could be more than a spatial resolution element. Thus to correct for this, MUSE uses an algorithm ([35]), taking parameters for pressure, temperature and humidity at the observatory to compute the refractive index of the air for a reference wavelength and using that for all other wavelengths in the data. The relative shift is calculated in both the spatial directions for each exposure taking into account the specific parallactic and position angles of the exposure and this shift is then corrected for all pixels and their corresponding coordinates in the pixel table.

2.2.4 Flux calibration using standard stars

Standard stars are used to derive the instrumental throughput which is a response curve used to flux calibrate the data and also to determine the spectrum for normalized telluric absorption. First, the pixel tables are merged, then divided by the flat field and a data cube is constructed with 1.25 Å /pixel as done for any science data. The

objects are detected using thresholding (like in the case of geometric calibration) to get initial positions for all possible stars in the FOV.

The flux of all the stars in this FOV is integrated over each wavelength plane and the PSF of this is expected to be a moffat profile [29] [21]. But, if a moffat profile is simply fit at each λ to extract the standard star spectrum, increased noise in the output spectra and a wavy continuum are expected. This is because changes arising due to noise often result in nonphysical differences while adjusting the wavelength planes. So the solution proposed to this problem is first, a free elliptical moffat is fit in all wavelength planes and then a second order polynomial is fit to the central position of the objects (This idea is validated from [24]). The wavelengths where this parameter deviates more than 3σ from the polynomial are rejected and then the moffat is fitted again at every wavelength plane, fixing the parameters to the obtained polynomial parameters and thus the only free parameters in this moffat which is refitted are the flux and the background level. So this smoothened moffat gives a high S/N ratio for the spectra for all stars in the field, but only 1 star is chosen, which can either be the brightest star or the one closest to the center in the FOV.

The wavelength ranges already known to be affected by the telluric absorption are marked and interpolated with a 2nd order polynomial. The fractional difference between the fit and the original data is the telluric absorption factor f_{tell}. The final response curve is obtained by extrapolating $s(\lambda)$ in eqn 1 to the largest possible MUSE wavelength range and then applying a smoothening function to it.

$$s(\lambda) = 2.5 log_{10} \frac{d_{ct}(\lambda)}{t_{exp} \delta\lambda f_{ref}(\lambda)} + f_{ext}(\lambda) A \tag{1}$$

Here, s is the sensitivity computed at each wavelength, d_{ct} is the recorded flux in counts, A is the effective airmass, f_{ref} is the reference flux, f_{ext} is the extinction curve provided by the user and t_{exp} is the exposure time.

The smoothening function to be applied is by default taking cubic polynomials on windows and then using a sliding average to reduce noise and reject outliers or by using a median filtration method. The pipeline uses the recipe *muse_standard* for this flux calibration using standard stars and it offers a way to change the selection of the star used for the calibration and the smoothening method.

2.2.5 Sky Subtraction

The sky subtraction in MUSE can be done in 2 ways. The first method is to take the science exposure, determine the sky in it and subtract it from that exposure. The second way is to observe sky fields that are offset to the science exposure and make the sky background characterization in that offset fields and then subtract it from the exposure. The only real difference between these two approaches is when the sky is created and subtracted, but the rest of the procedure is quite similar. For the data in the thesis, the first approach is used. The first approach would mean that the sky is decomposed once and assumes that during the observation the sky lines don't change too much and so their flux doesn't vary significantly during the time period of an observation, which given the exposure time is a valid assumption. While, the second method assumes the fluxes of the sky lines change significantly during an observation.

The module *muse_create_sky* is used to fit telluric emission lines. MUSE divides all possible lines in the wavelength range of 3129 and 11000 Å into 52 groups. Most of these lines and groups correspond to the OH molecule and lines are grouped together which are approximately varying in flux together. Some other line groups are formed from O_2 molecule, O and selective Nitrogen, sodium, potassium and Helium lines. Lines outside of the wavelength range and having flux less than 5 orders of magnitude of the strongest line are removed during the fitting process, so typically around 4000-4500 lines forming roughly 40 groups are used. The reason for using groups of line is that the fit to the fluxes is stronger as many of the lines are unresolved at the resolution offered by MUSE.

The fluxes of the group and their relative wavelength correction are then fit. The brightest line in each group is identified and its pixel value at the corresponding wavelength position is used. The minimization is done in a differential manner where spectral residual s(p) is calculated using intensity difference in neighbouring pixels from the formula:

$$s^2(p) = \sum_i \frac{[\delta I_m(\lambda_i, p) - \delta I(\lambda_i)]^2}{(\sigma_i^2 + \sigma_i + 1^2)\delta\lambda^2} \tag{2}$$

where $\delta \mathrm{I}_m(\lambda_i,\mathrm{p})$ is the difference in modeled intensity between two neighbouring spectral bins i and i+1 which include fit parameters p and σ_i^2 is the estimated variance

at each spectral position. The LSF for all lines is also taken into account when creating the sky spectrum.

For the sky subtraction on the science data, the pixel tables are merged for all IFUs, divided by the flat field and corrected for the atmospheric refraction. Additionally the correction for Raman lines is performed and autocalibration is done if given. A datacube is constructed from the pixel tables as well as a white light image which is thresholded with the threshold value as 5%. The skylines and their fit are taken, this continuum is taken for each wavelength for each entry in the pixel table and then subtracted from the data. It is done separately for each IFU and slice. This is the procedure described for the pipeline that can be used, but an alternate method, the zurich atmospheric purge (ZAP) can also be used and is described in section 2.3.6.

2.2.6 Astrometric calibration

The geometric calibration performed in pre-processing corrects for offsets per slice, but a need for calibration in the overall distortion and pixel scale is there which is performed with astrometric calibration. This uses astrometric fields whose imaging has been done by the Hubble space telescope (HST) and thus their catalogs are available.

We start with merging the pixel tables, then the astrometric fields are divided by the flat field, and a cube is reconstructed containing a stellar field of medium density. The distortions in the field are considered achromatic and thus to improve the S/N ratio, a large sampling of 50 Å pixel are used. Wavelength planes are combined using median values to remove any artifacts or cosmic rays. A threshold σ value is used to detect reference stars and a moffat profile is fit to give more accurate position of these detected reference stars. These reference stars positions are then compared to the HST catalog by 2 dimensional pattern matching [19], where 80% of the detections have to match a catalog entry within a selected radius. All these matched objects are then used to fit a six parameter astrometric solution taking into account their zero point positions, two scales, rotation and shear. The fit also uses a σ-clipped rejection method to reduce the effect of stars in the foreground of the clusters. This calibration can then be applied to the science data and is done with the *muse_astrometry* recipe in the pipeline.

2.2.7 scipost

The creation of the final cube is performed by post-processing the calibrated data and is done with the recipe, *muse_scipost*. The first step is to merge all the pixel tables from all the channels to a single table. This step uses the twilight sky cubes created in the pre processing step as an efficiency factor for each IFU which is applied as a scaling factor relative to the first IFU. This way the merged pixel table takes into account the efficiency of each IFU and doesn't introduce any new variabilities in the data. The next step is to divide by the flat field, but sometimes removing the large scale flat field can re introduce some variations at the small scale like telluric absorption or interference fringes, so a flat field spectrum is averaged for each IFU is taken and then science data is divided by this spectrum instead to not re introduce the small scale variations.

Then the merged pixel table divided by the flats, is put through the atmospheric refraction correction and flux calibration converting the pixel table data into flux units and if needed the Raman line scattering correction and autocal features can be used. Next the sky subtraction is done on the data, for which the pipeline provides several different modes. In the context of the data used in this thesis the mode 'auto' is used from the pipeline, where if dedicated sky observations are available for the object, the pre-calculated sky lines and continuum are subtracted and if they are not available, the sky is computed on a fraction of the FOV and then subtracted. For our data, this second option is selected by the pipeline. A sky fraction of 0.2 is used. While not precise, this is sufficient as no substantial artefacts are detected in the final cube and a second sky subtraction with ZAP is done later as mentioned earlier.

The next step is to correct for the telescope's motion which is generally done relative to the barycenter of the solar system. For this purpose, algorithms from G.Torres and the FLAMES pipeline [30] and transformations from [40] are used. The correction for spatial coordinates is then done with the astrometric calibration. All these corrections and calibrations are applied at the pixel table level and finally we obtain a combined pixel table that is corrected and calibrated through which a final reduced data cube is built for the exposure along with a white light image.

2.3 Combination of exposures

The combination of exposures is done by the pipeline after the muse scipost recipe, using the recipe *muse_exp_align* and the recipe *muse_exp_combine*. So before the combination is done, the offset for the different exposures needs to be estimated.

2.3.1 Exposure offset

When combining multiple exposures, specially the way the data is taken for these observations as show in fig 3, an offset needs to be applied to correct mainly for the pixel coordinates. For this purpose, a reference exposure is selected and the relative exposures offsets are measured with respect to the chosen reference exposure (calculated in arcseconds). First, the FOV or white light image or all the exposures involved are taken and the relative offsets are measured by following a procedure. In this procedure, first, the DAOPHOT algorithm [45] is used to detect sources in the FOV and the parameters for these sources are fine tuned, especially the FWHM, the sharpness and the roundness. The detected sources are sorted through a thresholding algorithm which does an iteration taking into account the thresholds utilised in the previous iteration steps and thus some sources are discarded based on these thresholds and sources near bad pixels are also discarded.

Thus a list of the sources for all the input exposures is created. Taking two exposures images at a time, the reference exposure and the exposure for which the offset is to be computed, a search is done with implementing a search radius decreasing at every iteration. At a given search radius, a pairwise combination is made for relative offsets between two detected objects in RA and DEC and the procedure is repeated at the next iteration by decreasing the search radii and taking every possible combination of the two fields. The offsets measured this way provide the relative offset of the two exposures and this process is then repeated for the other exposures to get their relative offsets as well.

2.3.2 Combination recipe

After measuring the offsets, the recipe *muse_exp_combine* can be used to combine the exposures which needs the offset file as one of its parameters to combine multiple exposures. The other parameters are the merged pixel tables for the exposures obtained

by the recipe *muse_scipost*, and the white light image with respect to which the offsets are taken.

The recipe loads each pixel table for each exposure, then uses a weighted function to compute the weight of each exposure relative to their exposure times. It takes the RA and DEC coordinates and corrects the offset for each exposures, it resamples the cubes to FITS format and computes the size of the final cube. It then overrides those values adjusting it to the size of the FOV image taken and then using median statistics applies the cosmic-ray rejection method implemented by the pipeline. After, it starts resampling using the drizzle method and finally produces 2 output files, a combined FOV image and the final combined data cube.

2.3.3 Cosmic ray rejection

Cosmic rays contain high energy particles, which can contaminate parts of the data to give false values. While cosmic ray events might be rare, they frequently happen in the Earth's atmosphere and thus must be accounted for to give an accurate representation of the data.

The way the pipeline handles this is very efficient as with 3D data, there are certain advantages that are utilized as opposed to 2D data, where a pixel would have 8 neighbours in the data cube. Here for 3D data, a pixel has 26 neighbouring pixels and these pixels are reconstructed from raw CCD based images, which can be very far from each other. Additionally to construct the 3D grid, there's often multiple exposures stacked on each other.So if a cosmic ray is striking one part of the CCD in a single exposure, most likely, the reconstructed pixels from different slices of the CCD will not have the same contamination in the adjacent pixels.

The pipeline constructs several grids of pixels and their adjacent pixels, then assigns a σ level with respect to the median value and all pixels in their respective grids above this level are marked as cosmic rays. For a single exposure a 15σ cutoff value works well, while for multiple exposures, a tighter window of 10σ is chosen. For the data used in the thesis, while combining exposures a 10σ threshold is chosen for cosmic ray rejection. Additionally, this process is improved as if the angle between the input data and the constructed grid is a multiple of $90° \pm 5$, it can be determined which pixels are originating from the same slice in the CCD and thus for the construction of

the grid, the pipeline will ignore those pixels if they are neighbours.

2.3.4 Drizzle resampling

Drizzle resampling is used during the combination of the frame and allows to get a better sampled PSF. It is a resampling algorithm, used to compute the weight of a pixel using its overlap with a voxel (A 3D element) in a constructed grid and is used for combination of images where each pixel is assigned a weight, so the combination can occur using pixel weighted functions. For context, a pixel can be thought of as a datapoint on the CCD, while a voxel would be a datapoint on the data cube, and a spaxel would contain multiple voxels or thought of as a spectrum in the datacube. This algorithm is inspired by the HST imaging (inspired by [16]), but unlike in HST where the pixels are forming a continuous image and are next to each other, here, the pixels are not regularly placed in the constructed grids and due to the size of the data, each pixel's size and position cannot be tracked, so an assumption is made that the pixels have the same size and their rotations are negligible respect to one another.

The formula to compute each pixels weight is then:

$$\mathrm{t} = \begin{cases} max[t_{out}, 0], \ if\, t_{out} + dt \leq t_{in} \\ max[(t_{in} + t_{out})/2 - dt, 0], \ otherwise \end{cases}$$

here, t= one of three coordinates (x,y,z)
t_{in} = input pixel size
t_{out} = output voxel size
dt = distance b/w the centers of input pixel and output voxel

total drizzled weight w for an output pixel is then computed as:

$$w = \prod_{x,y,z} \frac{max[t, 0]}{t_{in}} \tag{3}$$

2.3.5 Combination

The pipeline recipes *muse_exp_align* and *muse_exp_combine* were not working correctly and so multiple exposures were not directly combined with the pipeline. Instead, the esorex command lines were used. The steps followed for the combination are as follows:

- 3-4 exposures were taken together to be grouped to be combined depending on the configurations used and the selected exposures to create a merged data cube of the exposures
- a .sof file was created containing the names of the white light FOV images of the set of exposures to calculate the offsets respect to the first FOV image in the .sof file.
- using esorex command line for the *muse_exp_align* recipe, the OFFSET_LIST file was obtained which provides the offsets.
- another .sof file was created containing reduced pixel tables of the set of exposures, the offset list and the white light image with respect to which the exposures were taken so the final combined cube would adjust to the coordinates of the chosen white light image.
- Again, using the esorex command line, a final reduced data cube was obtained for the set of exposures chosen. In total, 5 final data cubes were obtained by grouping different exposures through this process.
- ZAP (section 2.3.6) was performed for these 5 cubes and then using the python module MPDAF [32], these 5 cubes were then combined using 2 different methods to obtain 1 final data cube.

The final data cube obtained from MPDAF presented 2 choices of combination, either through a mean σ-clipped method or through using median voxel. The results of both methods were compared by taking variance in a part of the cube where no object seems to be present. Both of these combination methods seem to give similar results and so for this work, the σ-clipped method was chosen but combining using a median voxel would have been a valid method as well.

2.3.6 ZAP

The description of ZAP done in this section is based on [44]. ZAP is a PCA (principle component analysis) based technique for MUSE to remove sky residuals from the data. Due to the nature of integral field spectroscopy, data in MUSE is split into channels which is further split into slices (section 1). The light path varies from slice to slice and channel to channel which introduces small discontinuities in the LSF, the wavelength

solution and the masterflat in the calibration process. MUSE introduces an advanced sky subtraction process but it functions on knowing the precise values of the LSF and the wavelength solution which is not possible due to these small discontinuities that are present. Thus over-subtraction or under-subtraction can occur of a sky model or interpolated sky emission spectrum when applying this to the data and as a result residuals are left behind for the sky emission lines which need to be removed as they can contaminate the science data.

Sky residuals are likely to be correlated over a small range of wavelengths within a given spectrum. PCA uses the data itself to describe the variations over the entire dataset, ranking them in their contribution to overall variance. Thus a PCA based approach, where this small range of wavelength contributes as a major source of variance for the data is ideal for use here.

Through PCA and filteration methods, ZAP constructs a sky residual spectrum for each individual spaxel which can then be subtracted from the original data cube and the steps to how it does it are described below:

1. Astronomical signals in the data cube are reduced or even eliminated by filteration techniques and/or masking methods, obtaining what are called 'clean' spectra.
2. On these clean spectra, ZAP performs SVD(singular value decomposition) simultaneously in a set of discrete spectral segments, referred to as eigenspectras over the entire wavelength range of the data cube.
3. Using these eigenspectras, ZAP calculates eigenvalues for each individual spectrum by applying a second weighted median filter to further remove any astronomical signals present in a spectrum.
4. ZAP calculates the overall variance within these subcubes associated to an eigenspectrum and correlates them with each successive eigenspectrum. These correlations help ZAP autonomously choose the optimum number of eigenspectra to use in the reconstruction of the residual spectra.

MUSE is estimated to have $\sim$ 90,000 spectra in a single exposure and this large number is an advantage to using this technique. ZAP constructs $\sim$ 3,680 eigenspectra for an exposure, but only about 2-3 % of these are used to reconstruct the sky residual spectrum. So, 2-3 % of the data is used to characterize 25 % of the variance which is

spectrally dominated by the sky residuals.

Hypothetically, ZAP can be run more on every single exposure since it relies on correlated residuals, but if too many eigenspectras are used for the reconstruction of sky residuals, it can de-noise the data, and some very faint astronomical signals can be lost. This has been observed to be the case for our data, and so ZAP is not used for every single exposure but the 5 final datacubes to be combined together as expressed in section 2.3.5.

An example of ZAP reduction with clear differences can be seen for one of the quasar images in an exposure in fig 8.

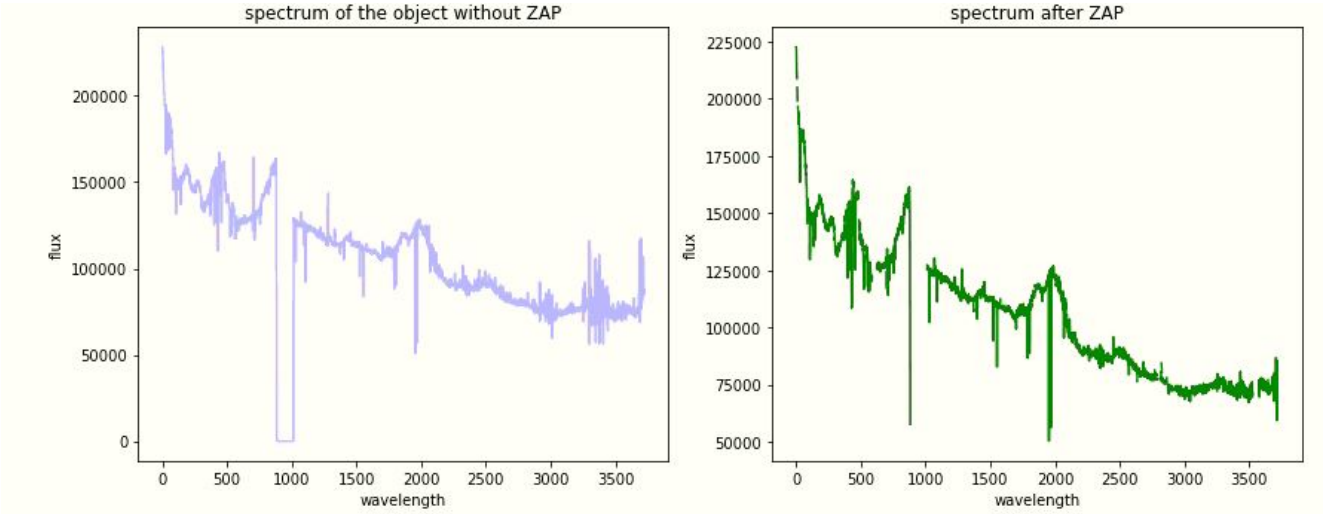

Figure 8: spectrum before and after ZAP sky subtraction is performed

2.4 Reduction summary

To characterize the reduction process in terms of the most important parameters through this work and what a user can expect to change/optimize fitting for their own needs, the tables 2, 3 are created for this work. All the parameters in the 'value' columns are default parameters of the pipeline and are used for this thesis. By visualising the data reduction process at various steps through images like figs 5, 6, 7 and the final white light images, data cubes, associated spectra and pixel tables through modules like MPDAF [32] in python, a need to change the default parameters has not arisen in this work.

Calibration	**Parameter**	**Default value**	**Alternative**	**Comments**
Bias (*muse_bias*)	Overscan	vpoly	offset	A polynomial fit works and is calculated with the pipeline, but the offset can be provided manually
Dark (*muse_dark*)	hotsigma	5σ	σ can be adjusted	This value is used to identify hot pixels for the bad pixel table, for this work, this seems to be working appropriately
Flat (*muse_flat*)	losigmabadpix	5σ	σ can be adjusted	Value above or below the σ-clipped mean determines the outliers
	hisigmabadpix	5σ		
Wavelength (*muse_wavecal*)	xorder	2	any	The horizontal order for the 2D polynomial which describes the curvature of arc lines in each slice of the CCD
	yorder	6	any	vertical order describing the wavelength-dispersion relation
	linesigma	2.5σ	σ can be adjusted	σ level for individual lines
	fitsigma	3σ	σ can be adjusted	σ level for final fit
	fitweighting	-	choose a line to give weight to	If needed, weight can be given to a particular line for the calibration
Geometric (*muse_geometry*)	sigma	2.2σ	σ can be adjusted	The σ level for spot detection
	smooth	1.5σ	σ can be adjusted	The 1.5σ level for the smoothening ensures no outliers are left
Twilight (*muse_twilight*)	lambdamin	5806.09 Å	-	The notch filter is applied to remove the noisy part obtained near the NaD laser region.
	lambdamax	5694.84 Å	-	
LSF (*muse_lsf*)	parameter	interpolation	Gauss-hermite	The Gauss-hermite function can be more accurate but its computationally more expensive

Table 2: Reduction table 1

Calibration	**Parameter**	**Default value**	**Alternative**	**Comments**
scipost (*muse_scipost*)	Raman lines	not used	Can be used	Since ZAP is used later, this is redundant for our work.
	autocal	not used	can be used as ='user', ='deepfield'	This is used when most of the sky background is blank, which is not the case for this data.
Flux using standard stars (*muse_standard*)	profile	default	multiple	The way to choose among multiple detected sources can be changed
	smooth	default	σ level can be adjusted	the smoothening behavior can be changed
Sky subtraction (*muse_create_sky*)	skymethod	auto	multiple	There are various ways in which the sky can be subtracted, but the default is ok for this work as an additional sky subtraction is done with the help of ZAP
	fraction	0.2	between 0-1	Part of the FOV considered as sky.
Astrometric (*muse_astrometry*)	detsigma	default	σ can be adjusted	Defines the σ level to use for object identification.
Cosmic ray (*muse_exp_combine*)	crsigma	10σ	σ can be adjusted	The cosmic ray rejection threshold
Resampling (*muse_exp_combine*)	resample	drizzle	Other resampling methods can be chosen	The drizzle-like resampling method here helps to conserve flux within the FOV.

Table 3: Reduction table 2

3 Extraction and analysis of spectra

After obtaining the best possible reduced data cube from the previous steps, the next step is to make a model for spectrum extraction with the goal to obtain the spectra of the lensing galaxy and of the quasar images.

The position of the lensing galaxy for the system 2M1134 is shown in fig 9 along with the labelling of the quasar images. The galaxy is several order of magnitudes dimmer than the quasar and so an accurate model of the 4 lensed quasars is needed in order to subtract the quasar images from the data cube to be able to obtain the spectrum of the lensing galaxy.

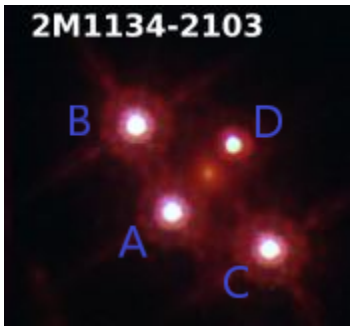

Figure 9: HST color image depicting the position of the lensing galaxy in the system 2M1134 [37]

For this purpose, I wrote a code focused on the quasar images. A 3D cube of the 4 lensed quasar images is fit to the data to extract the spectrum of the lensing galaxy as well as reconstruct the spectra for the 4 quasar images. The way it works is that first, a sub cube is extracted centered around the object whose white light image is displayed in fig 10. Next, a compound model of four bidimensional gaussians for each lensed image or four bidimensional moffats can be constructed to be fit on these lensed images of the quasar. As a first approximation, a model on just the 4 quasar images can be considered ignoring the lensing galaxy, although a more accurate extraction would require the modelling of the lensing galaxy as well. The reason the lensing galaxy can be ignored for this model is that it is very faint compared to the quasar images and its contribution is very little. Both a gaussian and a moffat profile were considered for the model and ultimately given the shape, the moffat profile was considered to be a better fit and chosen as a model to be fit based on chi square minimization.

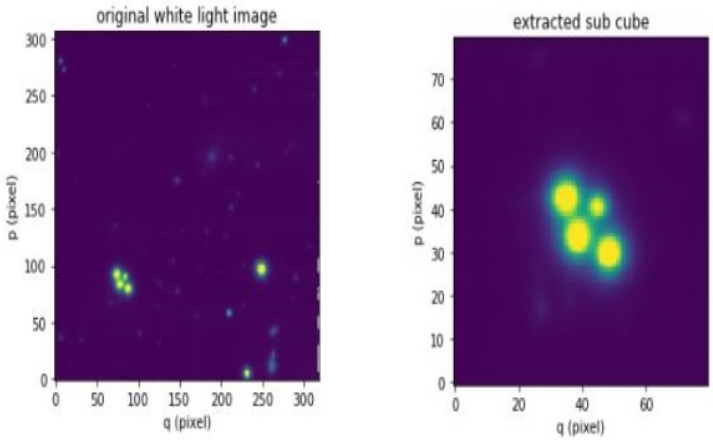

Figure 10: white light image of extracted sub cube

For a bidimensional moffat, the shape of the moffat profile can be given with the help of the equation :

$$f(x, y) = A(1 + \frac{(x - x_0)^2 + (y - y_0)^2}{\gamma^2})^{-\alpha} \tag{4}$$

Where, parameters to be taken into consideration are: [8]

- Amplitude(A) - The amplitude of the model
- x_0 - The x coordinate referring to the centre of the quasar image, or the maximum of the moffat model
- y_0 - the y coordinate referring to the centre of the quasar image or the maximum of the moffat model
- γ - the core width of the moffat model for the image on the FOV
- α- power index of the moffat model

To select the best PSF profile, all these parameters must be considered. A loop is defined to go through each monochromatic slice of the data cube, the fit is then evaluated for each slice and subtracted from it. The white light image of the quasar subtracted fit is shown in fig 13.

Several variations can occur from slice to slice and so first, the shape of the PSF depending on α and γ and the position of the centre x_0 and y_0 can slightly change for each slice. So for this purpose, to estimate realistic conditions for the fit, first the broad band image (fig 10) is worked on and its shape properties are derived. α, γ are then tied to the values obtained from this broad band image. The variation in position for each monochromatic slice done by the fit is shown in fig 11 and as we can see there is not much variation, thus the position parameter shows realistic conditions for the fit. The average of these positions with respect to image B from fig 9 obtained for the fit and converted to $\Delta\text{RA}_{arcseconds}$ and $\Delta\text{Dec}_{arcseconds}$ is compared in table 4 with the positions calculated for the HST data for 2M1134-2103 in [37].

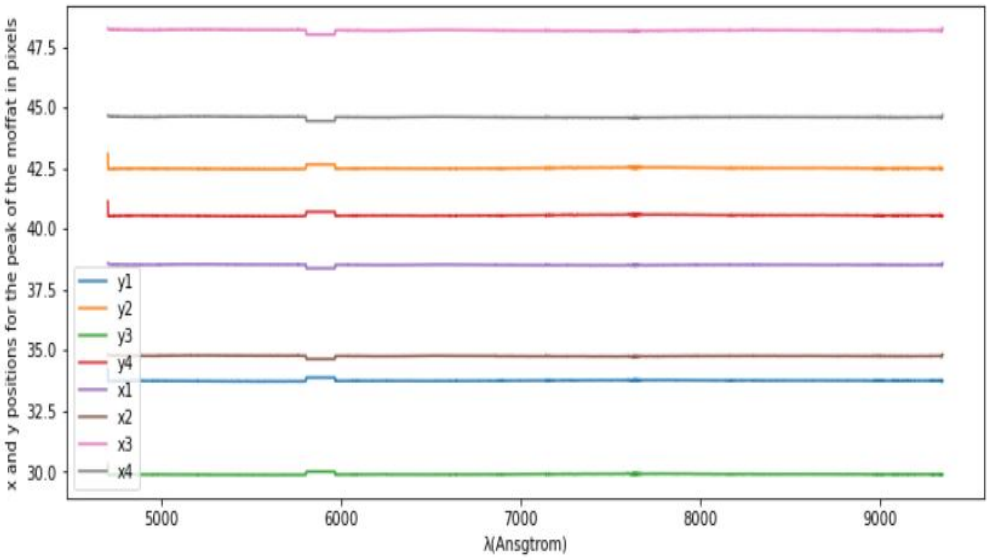

Figure 11: positions calculated by the fit for each monochromatic slice. Positions 1,2,3 and 4 correspond respectively to images A,B,C and D from fig 9

It can be inferred from the table 4, the positions are in agreement with the positions calculated for the HST data within 0.02 arcseconds.

The residuals give the quality of the fit and for each image the scaled residuals are plotted in fig 12. For image A, we observe residuals are scattered around zero with no obvious systematic trend, while a clear systematic trend in the red is observed for image B. If the data is noisy, larger residuals are expected which is observed in image D as it is the faintest image for the system and is more noisy than A. Larger residuals

image - -	**Δ RA** (HST) **[arcseconds]**	**Δ RA** (white light image) **[arcseconds]**	**Δ Dec** (HST) **[arcseconds]**	**Δ Dec** (white light image) **[arcseconds]**
A	0.733	0.750	1.759	1.749
C	2.682	2.681	2.534	2.521
D	1.986	1.966	0.385	0.388

Table 4: Relative position comparison with HST data

in red ($\lambda > 7500$) is observed for all images due to the large sky noise in that range and possible residual contamination from the lensing galaxy. These residuals suggest room to improve the extraction and one of the possible ways of doing so could be to model the lensing galaxy along with the quasar images.

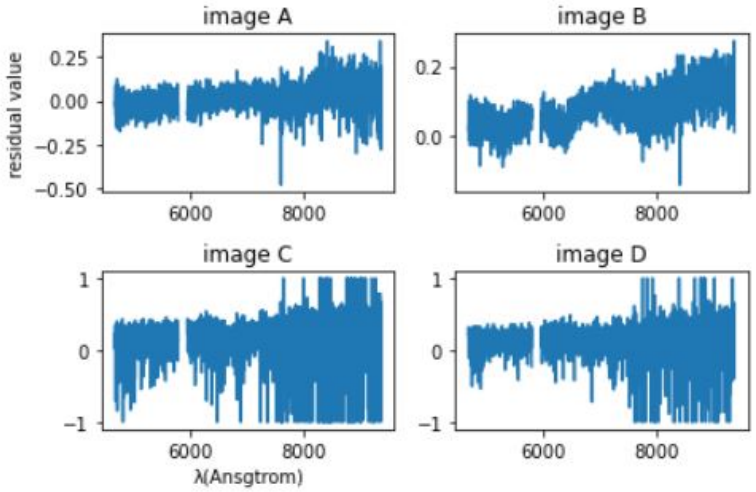

Figure 12: residuals for each image

Fig 13 is shown as the subtracted white light image obtained from the extraction, where LG (lensing galaxy) is marked in the center and galaxies in the field of view G1 and G2 are marked as well. The extraction is done by summing over the pixels for the datacube in a circular aperture of 2 pixels shown in fig 13. The result of the extraction performed above is 5 spectra, 1 for the lensing galaxy and 4 for the lensed quasar images. First, the spectrum of the lensing galaxy is analyzed.

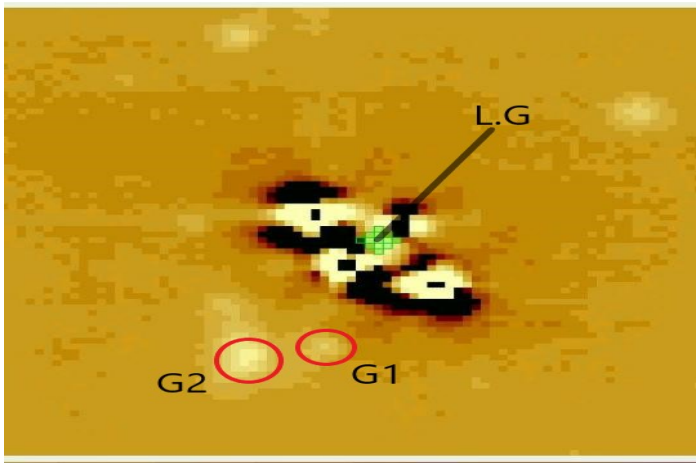

Figure 13: quasar subtracted white light image

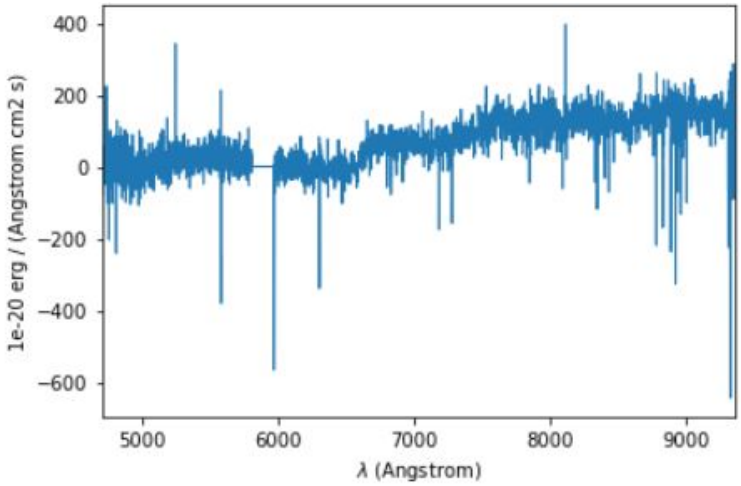

Figure 14: Spectrum of the lensing galaxy

3.1 Lensing galaxy

The spectrum of the lensing galaxy is shown in fig 14. The spectrum seems to be uniform with not much emissions but quite a few absorption features, which is typical for an elliptical galaxy. Also, emission above the noise is clearly apparent above 6500 Å and a clear break is detectable as one expects for an early type galaxy spectrum corresponding to the 4000 Å break, which is observed here as shown in fig 15.

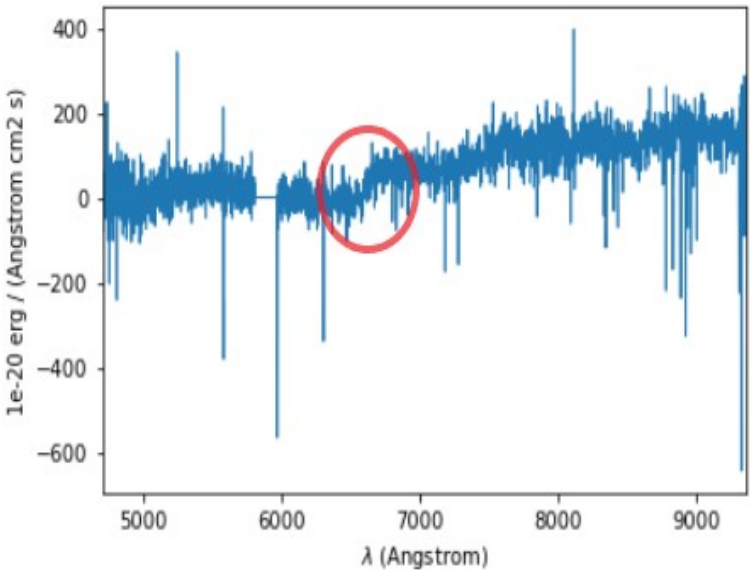

Figure 15: The 4000 Åbreak

Now that it is identified to be an elliptical galaxy, it could be nice to note in general a few properties of galaxy spectra. The continuum in the galaxy spectra which produces a mostly flat overall spectra results from the combination of spectra of the stars present in the galaxy, which are black-body spectra. The absorption features can be present due to atoms/molecules in the atmosphere of the stars present (mainly metals) that absorb at specific wavelengths and also due to cold interstellar medium. The emission lines can usually come from young stars and star forming regions or high energy atmospheres.

An elliptical galaxy will mainly have a continuum and quite a few absorption features as it is composed of mainly old stars and no galactic activity. The 4000Å break is prominent in elliptical galaxies as its caused due to absorption of high energy radiation from the metals in the stellar atmosphere, mainly Ca H and K [17]. This break can be seen clearly in the stellar spectra as observed in fig 15.

3.1.1 Redshift of the Lensing galaxy

Measuring the redshift of the lensing galaxy is one of the goals in this thesis. It allows to specify the lens properties, turn the einstein ring into a galaxy (projected) mass and is required to make use of the lens as a cosmological probe.

The way that the redshift is measured here is that first it is visualized using an elliptical galaxy template [47], by comparing the template spectrum to the spectrum of the lensing galaxy. After obtaining an idea of the redshift through this comparison, a more precise redshift is determined from absorption features of elliptical galaxies defined in [2].

Using the obtained redshift, we can obtain the rest frame spectrum as shown in fig 16. This figure shows the template of a elliptical galaxy and in comparison the spectrum of the lensing galaxy at rest frame wavelength obtained from the computed redshift. The lines for CaH and K and G band at 3934, 3969 and 4304 Å, are shown in the figure. These lines usually arise from the presence of cool old stars in the galaxy and are a good marker for elliptical galaxies.

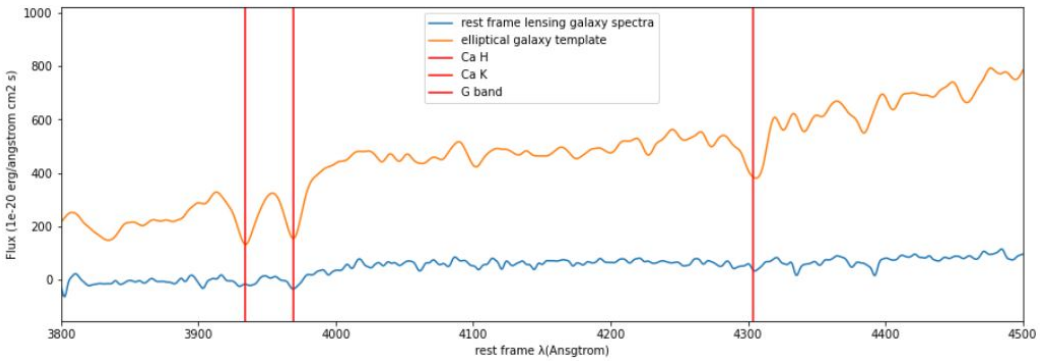

Figure 16: detected absorption lines in the lensing galaxy

The redshift is then given by :

$$z = \frac{\lambda_{obs}}{\lambda_{emitted}} - 1 \tag{5}$$

A 1D gaussian model was fit on these 3 absorption lines. For a 1D gaussian model, the parameters to be taken into consideration are : [8]

- Amplitude(A) - Peak value of the normalized profile
- Mean - The value where the peak is obtained
- stddev(σ)- the standard deviation of the gaussian

The shape of the gaussian is defined with the function:

$$f(x) = Ae^{\frac{(x-x_0)^2}{(2\sigma^2)}} \tag{6}$$

The mean parameter from the fit was considered to calculate the redshift and the arithmetic mean of these values was considered as the true redshift for the lensing galaxy. The standard deviation for these values is taken as the uncertainty on the determined redshift.

The redshift is found to be 0.6563 ± 0.00073.

3.1.2 Redshift of galaxies in FOV

It is important to know whether the galaxies in the FOV are in the foreground, background or more or less same redshift to the lensing galaxy. As they appear close in projection to the lensing galaxy, these galaxies visible in MUSE could impact the lens deflection and to quantitatively evaluate this impact, one needs to derive their redshift. Models performed by [34] indeed suggest that there is a source of shear south-east of the system.

In this context, we look at 2 of the brightest sources south-east of the system in the FOV as shown in fig 13 and their spectra is viewed to get their redshift. Measuring their redshift may help improving future macro model, accounting explicitly for those 2 systems. For instance if they are found to be at the same redshift as the lens, its likely to be a group of galaxies acting together than a singular massive lensing galaxy.

The spectra of the first galaxy (G1) is shown in fig 17. Some of its features are quite hard to distinguish, but the 4000Å break is clearly identified at 4957 Å as marked by the red line. Thus this galaxy has a redshift ~ 0.239 and is in the foreground of the lensing galaxy and judging by the absorption features seems to be an elliptical galaxy.

The spectra of the second galaxy (G2) is shown in fig 18. It seems to be an irregular galaxy with some emission features. The [OIII] doublet in particular is identified at 7349 Å and 7421 Å and the [OII] doublet is identified as well at 5522 Å and 5526 Å as depicted in the figure, thus giving it a redshift ~ 0.482 and also making it a galaxy in the foreground of the lensing galaxy.

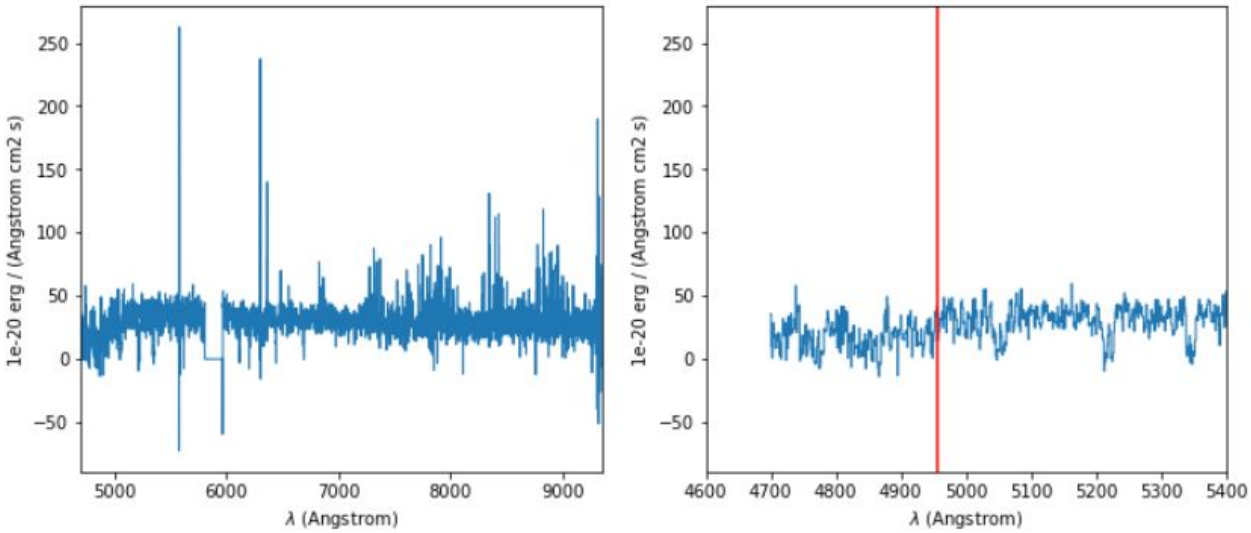

Figure 17: Spectrum of galaxy G1 in FOV with the detected 4000 Å break at 4957 Å

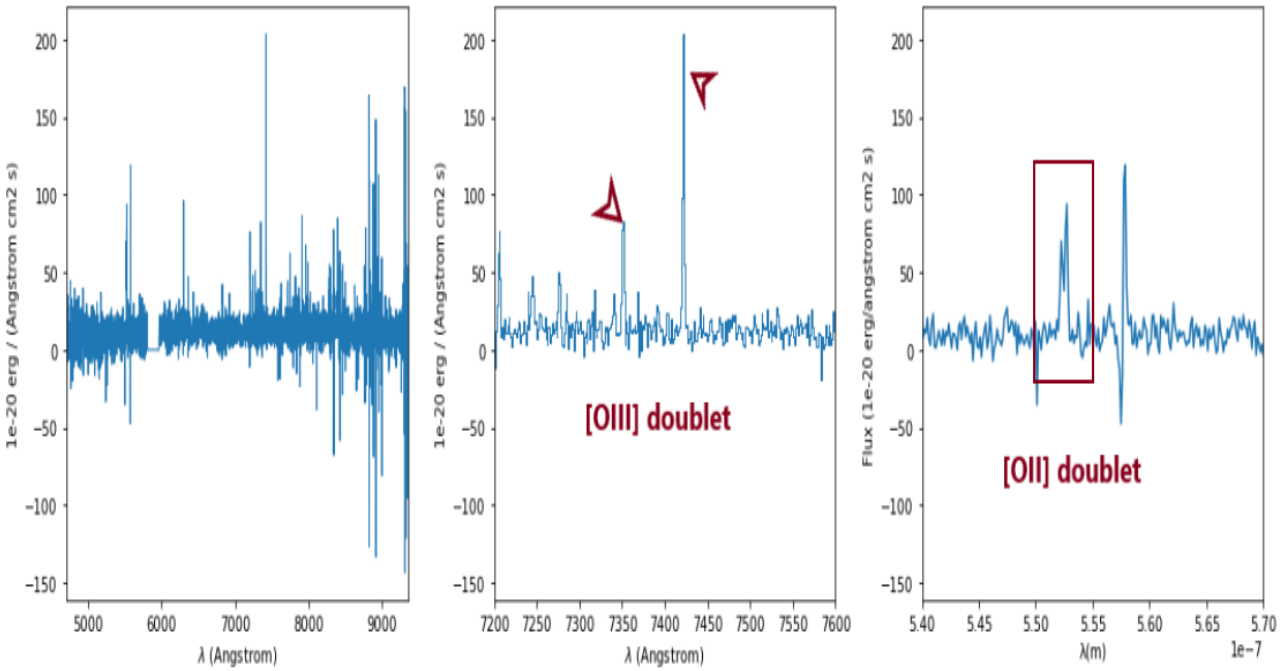

Figure 18: Spectrum of galaxy G2 in FOV with the detected [OIII] and [OII] doublets

3.2 Quasar Spectra

To understand the spectra of the quasar, a few things need to be understood first about the quasars themselves. Fig 19 [4] shows a typical AGN model showing various regions of the AGN and the types of AGNs observerd according to viewing angles.

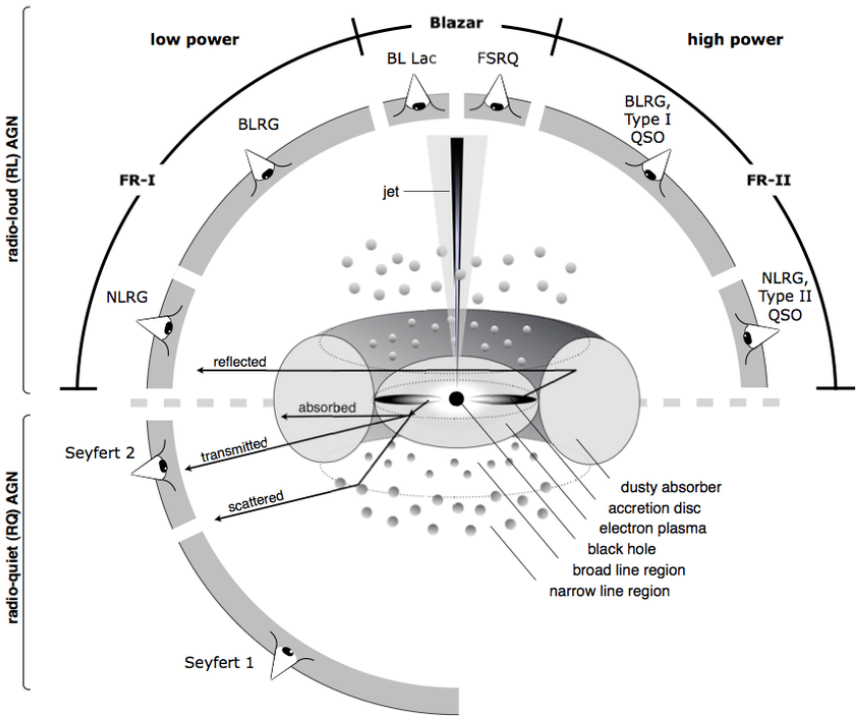

Figure 19: Unification model of AGN shown in [4]

At the center of the quasar, the supermassive black hole is present and around the black hole is the accretion disk which forms from the material flowing in towards the black hole. According to the α disk model (which is taken to be the standard accretion disk model considering a geometrically thin and an optically thick disk) [33], we can consider the disk to be made of several rings with small radii each acting as a blackbody emitter and is thus responsible for the continuum emission coming from the quasar. So, the continuum emission can be thought of as a superimposition of several black body emissions emanating from the accretion disk.

In addition to the accretion disk, there are a large number of small clouds orbiting

the supermassive black hole which make up the broad line region and the narrow line region as shown in fig 19. The clouds orbiting closer to the quasar generally have higher velocity, as the centripetal force given by mv^2/r is dependant on the distance. The clouds here, also tend to have higher density and this corresponds to the broad line region. Subsequently, the clouds further away from the quasar have lower velocity and lower density and correspond to the narrow line region. The broadening of the lines is due to turbulence and rotation around the central black hole [26]. The faster a region rotates, the more the line broadening.

The gas in these clouds can mainly be ionized in two ways, the first way being photoionization. High energy photons, released by the continuum emission from the accretion disk, interact with the neutral atomic/molecular species present in the gas clouds, ejecting one or more electrons and thus making them ionized. This is the main process of ionization for the broad line region as its much closer to the quasar. This makes for smoother profiles in the spectra and large line widths. The other process is collisional excitation, and for the narrow line region this plays a significant role as well and so we observe narrow line widths along with forbidden lines in the spectra. Since the density is lower in the narrow line region, probability for collisional de-excitation to occur is low [1].

As the spectra is observed from far away, there are also some gas clouds expected between the observer and the quasar which gives rise to absorption features in the observed spectra. The gas clouds will absorb some part of the light directed towards the observer and this provides a hint to the distribution of matter between the observer and the quasar. [1]

Thus as an oversimplification the main features expected to be seen in spectrum of the quasar is a blend of the continuum emission + broad line emission + narrow line emission + absorption features.

3.2.1 Redshift of the Quasar

First, a composite quasar spectrum was chosen at rest wavelength to identify some common emission lines to visualise the quasar spectrum and emissions [38]. This is displayed in fig 20. Certain quasar emissions in the spectrum resulting from CIV at 1549 Å, CIII] at 1908 Å and MgII at 2798 Å which are bright enough in the available

wavelength range can be seen as good markers to measure the redshift of the quasar.

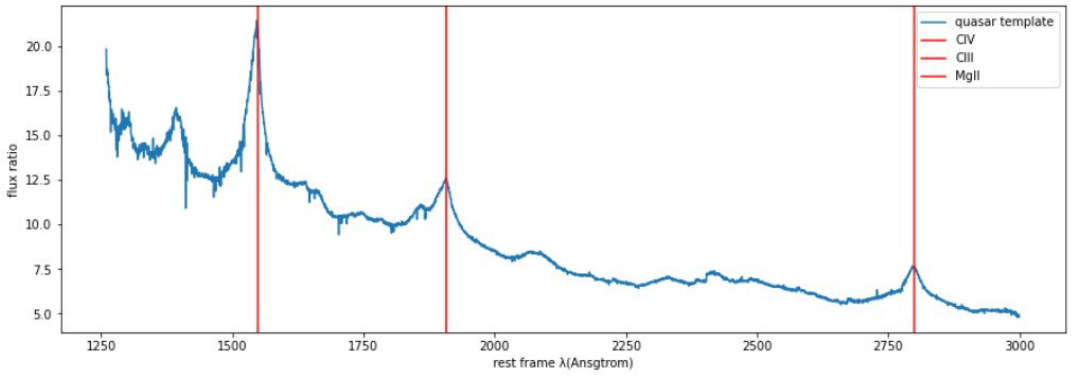

Figure 20: quasar template

The spectrum for 2M1134-2103 obtained is displayed in fig 21. The emission due to CIV falls in the part of the spectrum that is cut for the calibration of the laser guide star used for the adaptive optics and the MgII emission falls outside of the obtained spectrum. Thus in this work, the redshift is determined through the CIII] emission.

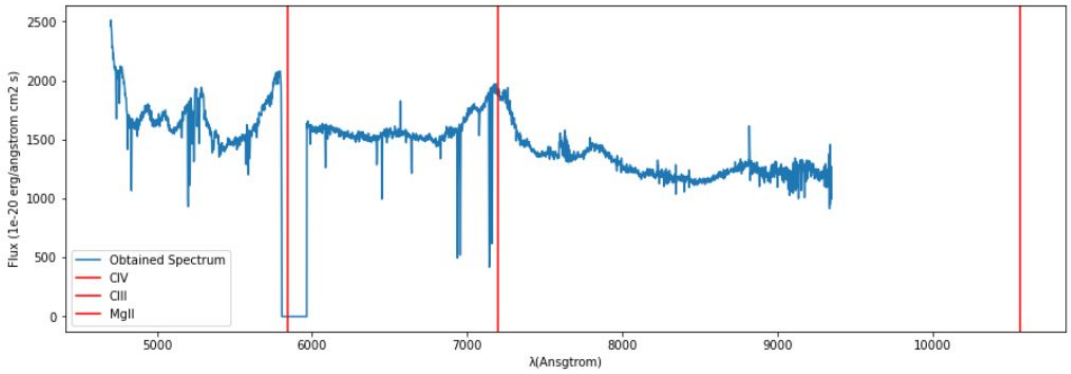

Figure 21: quasar spectrum for 2M1134

The quasar redshift is determined to be 2.77, which matches the value derived in [34] and [37].

3.2.2 Spectrum of the Quasar, detected emissions and absorptions

The spectrum of the quasar for each of the 4 lensed images in fig 9 is obtained from the extraction process and is shown in fig 22. The spectra A, B, C and D correspond

respectively to images shown in fig 9.

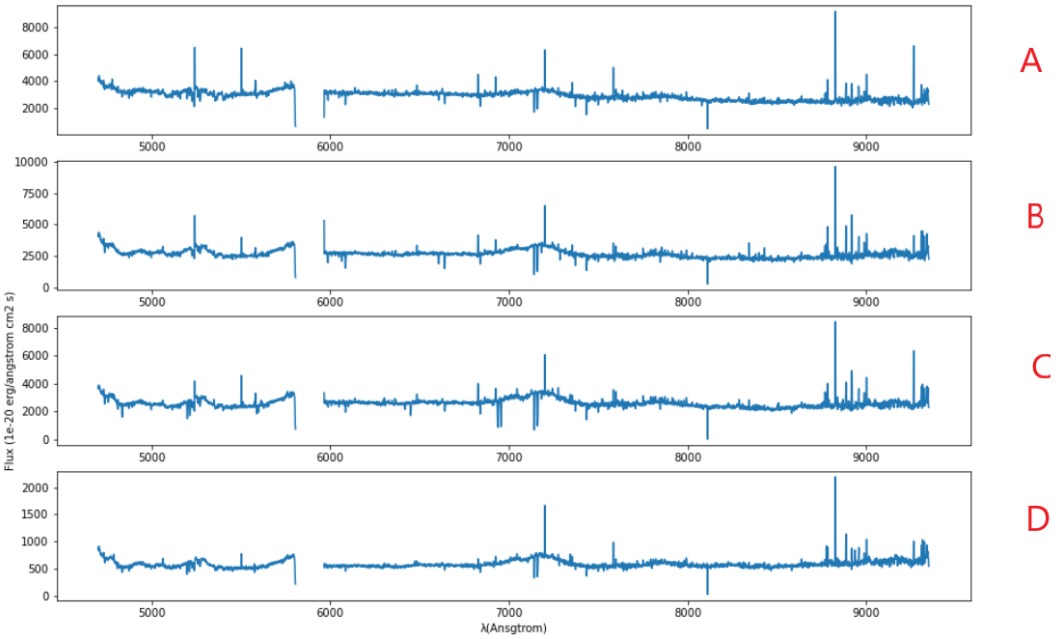

Figure 22: quasar spectrum
for each lensed image

The spectra are similar up to a multiplication factor with some additional tiny differences that are not apparent with fig 22. These difference could arise due to microlensing, time delays between the images, differential extinction. Spectrum C is chosen to further display the results for the detected emissions for the quasar as it is bright enough to observe the features needed. At a first look a blend of emissions for SiIV + OIV] around 1400 Å (5280 Å in MUSE data), is identified along with a blend of emissions from AlIII,SiIII] and CIII] around 1900 Å (7160 Å), as shown in fig 23 and the FeIII emission around 2039-2113 Å (7687-7966 Å).

Absorption features found in the quasar spectrum could hint to the material found in CGM (Circumgalactic medium) of galaxies foreground to the quasar which could help in the understanding of galactic evolution. [18]

The absorption features observed depend on the optical path taken, which is different for the different images of the quasar. Thus the absorption features observed in a spectrum could differ from other spectra depending on the position of the galaxy causing that absorption feature.

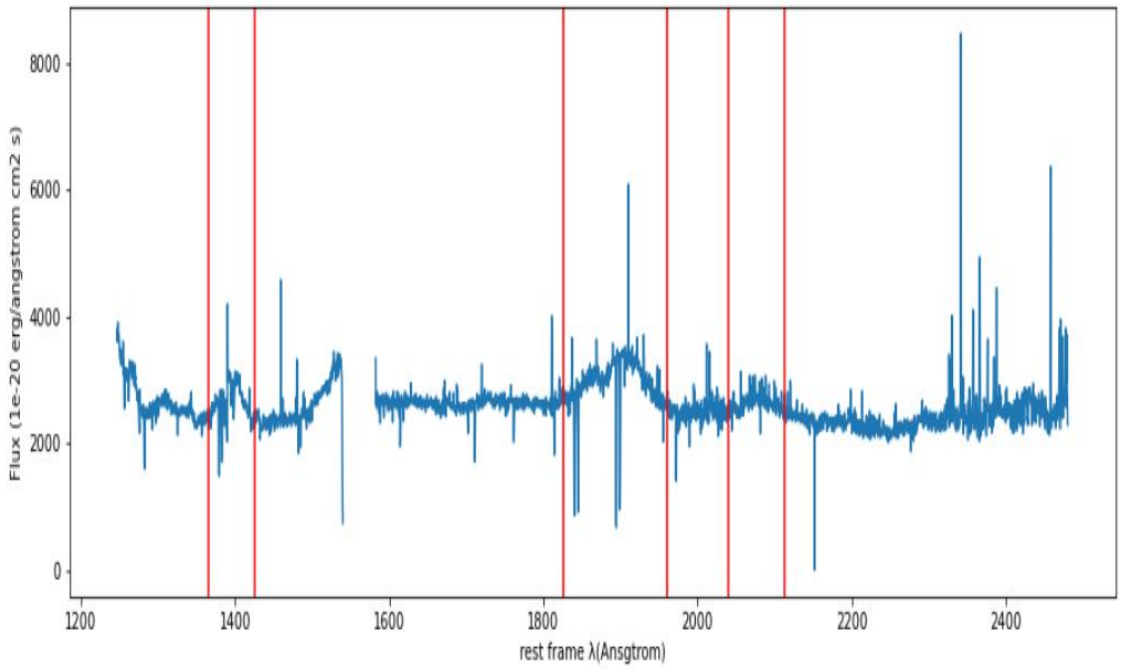

Figure 23: Identified broad emission lines around 1400,1900 and 2039-2113 Å

[34] in their work detected 2 absorption systems due to Fe and Mg emission lines, one at z=1.554 and the other at z=1.481. These absorption systems have also been detected in the spectra of our images. The absorption system at z=1.554 is displayed with the help of the spectrum B and is shown in fig 24, as the first system has stronger lines for image B. Similarly, the absorption system at z=1.481 is displayed with the help of spectrum C as it has stronger lines for image C and is displayed in fig 25. In their work, [34] mention that their is a possibility that these lines could be associated to the lensing galaxy which was not detected at the time, but concluded that the narrowness of these absorption lines makes it unlikely to come from the lensing galaxy. Since we detect the lensing galaxy at z=0.65 in our work, we conclude that these absorption lines indeed do not arise due to the lensing galaxy.

Table 5 summarizes the rest frame wavelengths of the lines whose absorption is detected in the MUSE spectra and are shown in figs 24 and 25.

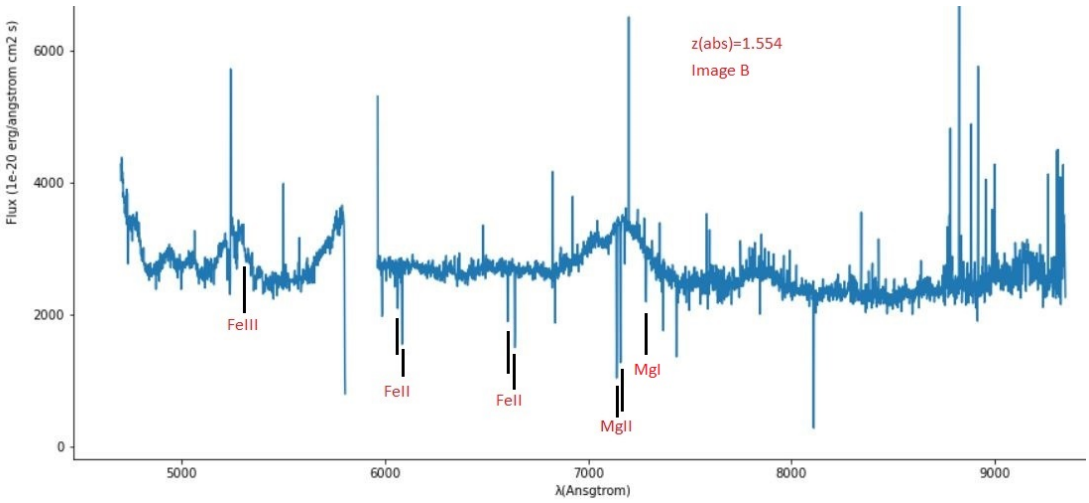

Figure 24: absorption feature at z=1.554 displayed with the help of spectrum B

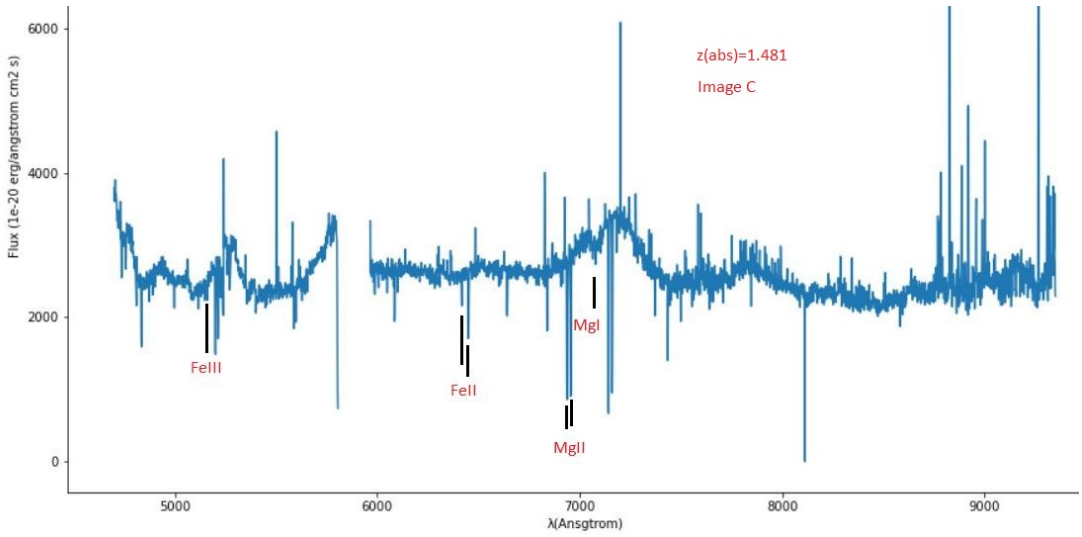

Figure 25: absorption feature at z=1.481 displayed with the help of spectrum C

Spectral line	**Rest frame λ**	**λ observed in MUSE spectra**
FeIII	2078	5155,5307
FeII	2373	6062
FeII	2382	6084
FeII	2586	6420,6604
FeII	2599	6450,6638
MgII	2795	6935,7138
MgII	2802	6952,7157
MgI	2852	7076,7284

Table 5: Fe and Mg absorptions detected in MUSE data for 2M1134-2103

4 Black hole mass estimation

The quasar as we know, contains a SMBH at its center. A SMBH typically has a mass of 10^5-$10^{10}M_\odot$ [3]. The mass of the black hole is an important parameter to be quantified as it has various applications in cosmology from understanding the evolution of the galaxy to accretion disk models. The size of the broad line region is linked to the mass, assuming the gas in the broad line region is virialized (the matter in the gas is assumed to have interacted and settled into equilibrium, allowing it to obey the virial theorem) and this is one of the ways of estimating the black hole mass.

One of the ways of measuring the black hole mass is called reverberation mapping (RM), it is a rather convenient method but can only be applied to a limited number of systems for which, dense and high SNR monitoring can be performed. As discussed in section (3.2), photoionization by the photons emitted from the accretion disk produces the broadened emissions observed for the broad line region.

The light from the accretion disk can vary in brightness and so the flux in the broad line region would vary strongly in response to the variation from the continuum emission and so it will 'echo' or 'reverberate' in response to the continuum emission [31]. But this response is not instant and is dependant on the distance travelled by the light to reach the broad line region, corresponding to the radius of the broad line region and this response is recorded in the function TF with the delay given by τ.

The correlation of these observed emissions in the BLR to the continuum emission from the accretion disk can be given by the equation given in[5]:

$$L(t) = \int \psi(\tau) C(t-\tau) dt \tag{7}$$

Here, L(t)=Emission light curve, C(t)= Continuum light curve and $\psi(\tau)$= One-dimension transfer function(TF).

The goal of RM is to use these observed light curves of L(t) and C(t) for an AGN and to solve the integral to obtain the function TF, thus getting information on the size and conditions present in the broad line region. A unique solution is rather difficult to obtain for TF. However performing a cross-correlation analysis between the light curves allows to find a lag (temportal shift) between the continuum and emission

line. For a single emission line, different segments of the line are formed at different effective distances from the ionizing source. For that case, the response in the flux of the emission line is caused due to a 2D transfer function called a 'velocity delay map' [20]. Different parts of such an emission line are studied with RM to derive the velocity field of the BLR gas [9].

Since we assumed that the gas is virialized, using Newtonian mechanics, a relation can be derived to calculate the size of the broad line region through this technique and would give the estimate on the black home mass through the relation, eqn 9.

Lets imagine a gas cloud in motion around the BH, the light from it would be blue shifted when facing the observer and red shifted while going away from it (with respect to the original redshift of the quasar) fig 26. The distance between the BH and the cloud can be taken as R, and then through Newton's gravitational law,

$$F = -\frac{GMm}{R^2} \tag{8}$$

Where G is the gravitational constant, M is the mass of the black hole and m the mass of the broad line region and so F is the gravitational force between them. Now, from Newtons second law of motion, F=ma. The acceleration here can be considered to be centripetal acceleration due to the effect of the BH and so a=-v^2/R. Using these relations, we can obtain eqn 9.

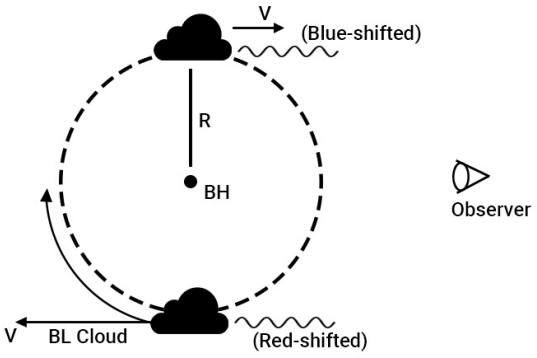

Figure 26: A BL cloud in motion around the black hole. credits: Zoe Alexander

$$GM_{BH} = fR_{BLR}(\Delta V)^2 \tag{9}$$

Where, f=form factor/virial factor (depends on the shape of the BLR and the viewing angle), R_{BLR}= Size of the broad line region and V=root mean square velocity obtained through assuming a maxwellian distribution of the gas clouds in the region. R_{BLR} and ΔV can only obtained through RM data. If RM cannot be performed (as it requires continous monitoring of the source for a significant period of time), one can use observational and theory supported relations between for eqn 9, where proxies are used for R_{BLR} and ΔV. A mass-luminosity relation can be used as a proxy for R_{BLR} and the line width of a broad line in a spectrum , its FWHM (full width at half maximum) is used as a proxy for ΔV.

The technique used in this work to derive the black hole mass is not RM, but scaling relations derived on the basis of RM observations. These scaling relations have been derived by [28] where they studied 39 AGN spectras. The way a scaling relation works in principle is firstly the size of the BLR is expressed due to the mass-luminosity relation and is given as:

$$R_{BLR} = K'(\lambda L_\lambda)^\alpha \tag{10}$$

Where K'= a constant and α typically has a value between 0.5-0.7. Using this equation in eqn 9 , the mass of the black hole can now be given by the equation:

$$M_{BH} = K(\lambda L_\lambda)^\alpha (FWHM)^2 \tag{11}$$

Where the new constant K now incorporates gravitational constant G and the virial factor f. Assuming the value of f as f=1 which can be a good approximation according to [49] for the Hβ emission, is used in the scaling relations derived by [28], as they derive it based on Hβ line. However, there can be huge uncertainties on f ($\sim$ 50 %) and so f can be different for different lines depending on the line properties (like FWHM,peak, line offsets) as well [39]. The FWHM corresponds to the measured FWHM of an emission line giving the ΔV of that emission.

In their work, [28], used the X-shooter instrument on the VLT to cover a spectral

range of 1500-7000 Å. They derived scaling relations for 3 emission lines and the luminosity at continuum emissions in the range of UV/optical. Mainly for:

1. The Hβ line at 4861 Å, and continuum luminosity at 5100 Å.
2. The MgII emission at 2798 Å, and continuum luminosity at 3000 Å.
3. The CIV emission at 1549 Å, and continuum luminosity at 1450 Å.

The rest frame MUSE spectrum of 2M1134-2103 corresponds to [1240,2480]Å, such that only the CIV emission can be used here to estimate the BH mass.

As discussed in the work of [28], the best line to estimate the blackhole mass is the Hβ line, and it can be shown that the MgII emission more or less originates in the same region as the Hβ emission and almost similar and accurate scaling relations can be derived for MgII. However, the CIV emission doesn't come from the same region and a major assumption used for the relations that the gas in the BLR is virialized might not hold true for the CIV emission, thus there must be some corrections applied to the scaling relations of CIV. Despite this caveat, and because no other lines could be used we have used that relation and associated correction in this work to infer the BH mass of 2M1134 through the works of [28] and their suggested corrections.

It is also noteworthy that the spectrum obtained in this work shown in fig 21, the CIV emission line falls in the part of the spectrum that is cut out due to the contamination from the laser guide star used for the adaptive optics and thus cannot be used. Hence, the spectrum obtained in the works of [34] is used instead, depicted in fig 27.

4.1 Detailed process

This section highlights in details all the steps involved and the approximations made to estimate the black hole mass for the quasar, 2M1134-2103.

The spectrum obtained in [34] had no absolute flux calibration and has been rescaled in flux based on the MUSE data from this work. Thus the spectrum with rescaled flux is shown in fig 27. Here, the spectrum obtained in [34] corresponds to image B of the quasar as shown in fig 9, and so careful consideration must be made that the derived scaling factor is from the same quasar image obtained in this work. The flux density is in cgs units of erg/s/cm^2/Å.

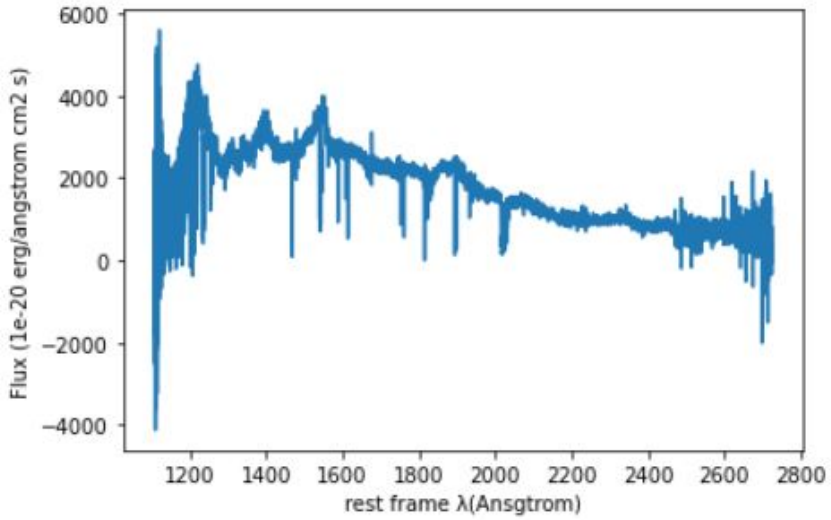

Figure 27: Spectrum obtained from the works of [34]

Given the units of flux density, the flux needs to be calibrated for mainly 3 factors:

1. Time dilation (/s)- The rate at which the photons are received at the telescope is slower than they were emitted by the source due to the time delay τ. For flux calibration it can be expressed as $F_\lambda/(1+z)$ [4].

2. Energy(ergs)- The energy of the observed photons is lower than the emitted photons considering the factor $F_\lambda/(1+z)$.

3. Bandwidth -Considering Flux density over a range of wavelengths, the range of wavelengths is wider than the range of emitted wavelength due to the redshift which means the factor $F_\lambda*(1+z)$ needs to be considered here.

Hence, finally using these 3 relations, we get the relation between $F_{\lambda,obs}$ and $F_{\lambda,source}$ as :

$$F_{\lambda,obs} = \frac{F_{\lambda,source}}{(1+z)} \tag{12}$$

The relation obtained in eqn 11 is a mass-luminosity relation and so, the flux density needs to be converted into a luminosity. Assuming a sphere of radius d, where the

observer is placed at d,(the distance) luminosity density (L_λ) in the units of erg/s/Å, can be obtained as:

$$L_\lambda = (F_\lambda * \pi * d^2)/M \tag{13}$$

Here, M is the correction for the magnification factor for the image B (obtained from the works of [37]) and d is the luminosity distance taken in cm, according to the cgs unit system used. Distances in an expanding universe of arbitrary geometry require numerical integration [27]. To obtain this distance a cosmological calculator developed by [50] was used where they automatically take the latest value for the H_0, Ω_m and Ω_{vac} and a flat universe model was considered.

This allows us to convert F_{1450} to L_{1450}, which is obtained as 5.38x10^{45} erg/s.

To calculate the black hole mass, the FWHM of the CIV line is needed as well. To isolate the broad line emission, first the continuum emission is fit and subtracted from the spectrum. The continuum emission is taken here as a local polynomial fit and is shown in fig 28 and finally the continuum subtracted emission is depicted in fig 29.

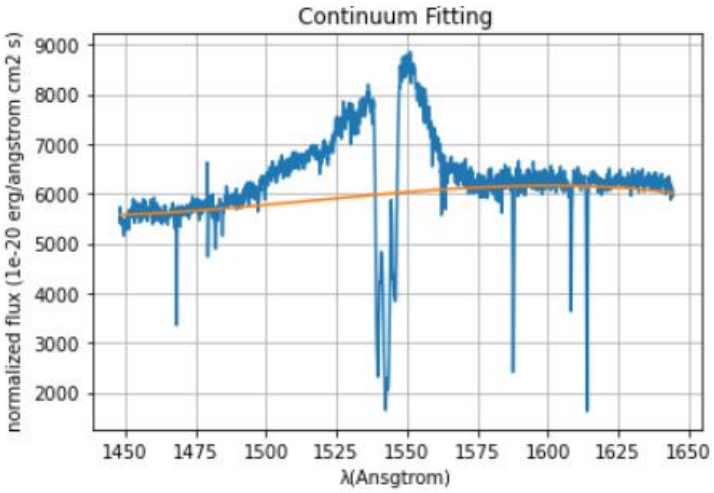

Figure 28: Continuum fitted on CIV emission

Finally, a double gaussian is fit for the emission, without masking the absorption as shown in fig 30 and the FWHM is noted as 8003km/s.

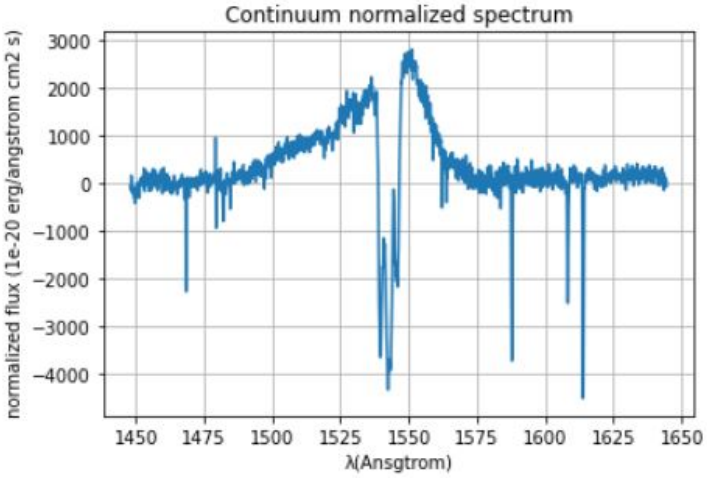

Figure 29: Continuum subtracted CIV emission

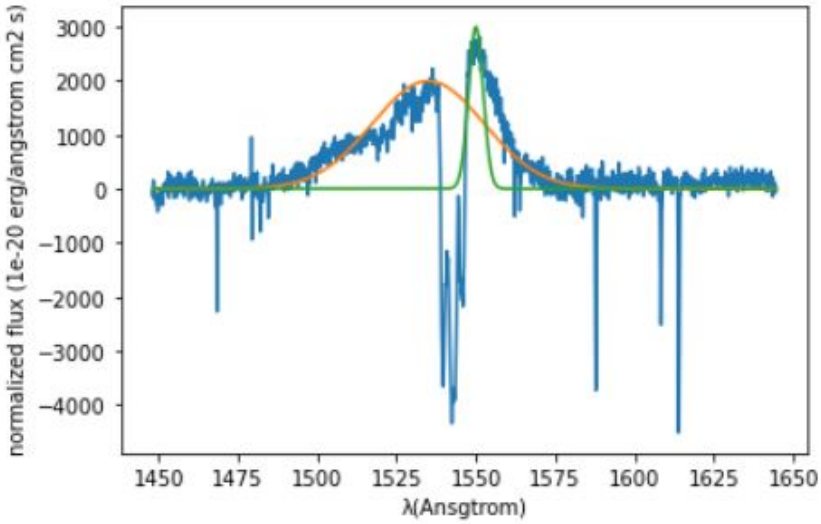

Figure 30: Double gaussian fit for CIV emission

[28] proposes 2 different corrections to derive MBH from CIV, each of them involving the peak luminosity of another line and can be given by the following equations:

$$M_{BH} = 1.13 * 10^6 \left(\frac{L_{1450}}{10^{44}}\right)^{0.57} \left(\frac{FWHM(CIV)}{10^3 kms^{-1}}\right)^2 \left(\frac{L_P(SiIV + OIV)}{L_P(CIV)}\right)^{-1.66} \quad (14)$$

$$M_{BH} = 5.71 * 10^5 \left(\frac{L_{1450}}{10^{44}}\right)^{0.57} \left(\frac{FWHM(CIV)}{10^3 kms^{-1}}\right)^2 \left(\frac{L_P(CIII])}{L_P(CIV)}\right)^{-2.09} \quad (15)$$

For these relations, the luminosity peaks of the detected CIII] line and SiIV+OIV lines are used, and their peak is identified by fitting a gaussian and the peak of the guassian models are taken.

The M_{BH} calculated through eqn 15 is 3.305x$10^8 M\odot$.

Generally, the CIII] line is better for calculating the mass than the SiIV+OIV line. But, calculating this mass there are quite a few uncertainties involved on the estimates of the black hole mass. Some of the random sources of error are:

1. The noise in the spectrum obtained affecting the fits.
2. Microlensing present in the spectrum used as it can magnify or distort the image and thus the flux observed could be vastly different from the flux from the source.

And some of the systematic sources of error in the work could be:

1. The CIV line scaling relation not being as reliable as the Hβ or MgII as it does not originate from the same region as the Hβ and MgII emission in the BLR.
2. Fe emission is a broad line emission that's blended in the whole spectrum, its not been estimated and subtracted in this work, but doing so could help reduce the systematic uncertainty.
3. Error in the flux calibration process.
4. Uncertainty on the Gaussian fit made to calculate the FWHM.
5. Uncertainty on the distance calculated through the cosmological constants that are used.

The microlensing effect is explained and worked on in section 5. From the results of section 5, it is clear that there is no microlensing detected for the spectrum B, which is used to calculate the black hole mass and thus no correction is needed due to this effect.

The largest source of error is the one from the scaling relation and it amounts to 0.33

dex on M_{BH} [28]. We use this value as a minimum uncertainty on the black hole mass. Hence, $\log(M_{BH}/M\odot) = 8.519 \pm 0.33$.

Considering M_{BH} another important property, the R_{BLR} can be derived using eqn 24, thus estimated R_{BLR}= 6.85079x10^{14}m.

5 Microlensing

Einstein in [12], studied the effect of gravitational lensing for a star acting as a lens on another star as a source, and concluded that there could be multiple images produced for the source, with the same principle as strong lensing (macrolensing). However, they would not be able to be spatially resolved for such small objects. But this nevertheless can cause change in the brightness of the source

The signature of microlensing is a change in time over apparent brightness of an object. One of the ways to study this effect would be to monitor a target for a long period of time, and compare the lightcurves of the individual lensed images. For gravitationally macrolensed quasars, where multiple images of the same quasar can be observed, stars in the lensing galaxy can act as individual minilenses to produce microlensing effects in one or more of the quasar images. This was predicted in 1979 by [6] and a first such microlensing detection for one of the images of the macrolensed quasar system, Q2237+0305 was made in 1989 by [23]. Quasars are variable objects and any fluctuations caused by the intrinsic variability of the quasar would show up in all of the macro-lensed images of the quasar, thus fluctuations present in an individual lightcurve of a macro-lensed image which are not present in the other lightcurves of the other macro-lensed images can safely be credited towards microlensing [36]. In this section, microlensing is explained in the context of as happening in a strong lensed quasar.

Looking at the principle of gravitational macrolensing, the system involves a source (S), a lens (L) and an observer (O) as shown in fig 31, with various angles depicted in the figure, along with various angular diameter distances. The light emitted from the source is deflected by the lens, multiple images of the source are produced which can be observed by the observer in directions corresponding to slope of the incoming light rays.

A thin lens approximation is considered here, where it is assumed a clump of matter is responsible for most of the deflection of the incoming light rays from the source at a single distance.

From fig 31, a relation can be derived which is written as :

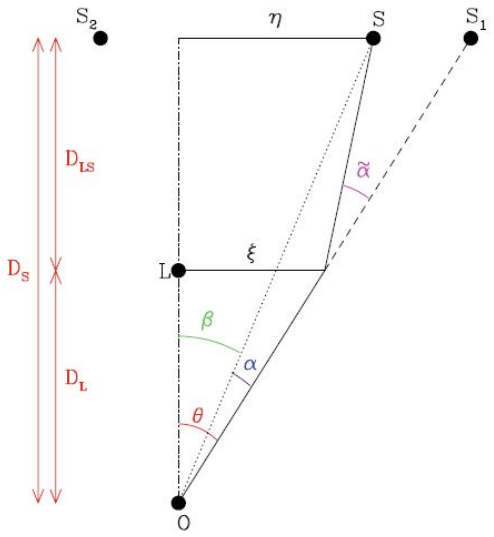

Figure 31: A gravitationally lensed system. credits:[36]

$$\theta D_S = \beta D_S + \tilde{\alpha} D_{LS} \tag{16}$$

and for θ, β and $\tilde{\alpha} \ll 1$, which is a condition that is generally fulfilled in every astrophysical situation, the lensing equation can be derived considering a reduced defection angle α as:

$$\alpha(\theta) = (\frac{D_{LS}}{D_S})\tilde{\alpha}(\theta) \tag{17}$$

The lensing equation can then be written as :

$$\beta = \theta - \alpha(\theta) \tag{18}$$

For a lens of mass M, the deflection angle (α) can be calculated and for a special case where the source exactly lies behind the lens (hence β=0), a ring-like structure appears whose radius is called the Einstein radius (θ_E) and is expressed as:

$$\theta_E = \sqrt{\frac{4GM}{c^2}\frac{D_{LS}}{D_L D_S}} \tag{19}$$

For a lens and source at cosmological distances using eqn 19, taking z_L=0.5 and z_S=2 (which are the respective redshifts for the lens and the source) as a general approximation to visualise the spectral resolution needed in arcsecs to be able to see multiple spatially resolved structures, θ_E can be expressed as :

$$\theta_E \approx 10^{-6}\sqrt{\frac{M}{M\odot}} arcsec \tag{20}$$

Thus, generally the ring produced by the stars as a lens cannot be spatially resolved even with the best telescopes available. A mass of $\approx 10^{12}$, which is typically the mass of an elliptical galaxy is needed to spatially resolve the images by 1 arcsecond and can be distinguished and resolved with current telescopes, which is the case for gravitational strong-lensing for 2M1134-2103 system studied in this work.

Thus microlensing occurs when the lens is of the size 10^{-6}-10^{3}M$\odot$, which would produce multiple images of the source in the form of an Einstein ring, but since they cannot be spatially resolved it would appear as a change in the brightness of the source. The lens in question can be anything range from a planet to a star to even a stellar mass black hole as long as it is within this physical limit. The object in most cases is a part of the lensing galaxy, but in theory could belong to a different foreground galaxy or even a free floating object. In this work it is assumed to be a part of the lensing galaxy. The observer, the lens and the source are all in relative motion and so the total magnification, which is the sum of all the micro-magnifications of all the micro configurations changes with time which makes gravitational lensing a dynamical phenomenon [36].

A microlensing event is highly dependant on the source size and a particular region of the AGN can be magnified if the size of the region in question is comparable to the Einstein radius of the microlens. Thus if the source size is too broad in comparison, it is less likely to detect microlensing in that region, as the effect of all the micro-magnifications averages out over the source. This is usually the case for the narrow line region. For the broad line region and the continuum, the source sizes are usually comparable or smaller than the einstein radius.

The way this comparison can be made is by projecting the Einstein radius onto the source plane, giving it a size R_E, shown in eqn 21, derived from eqn 19.

$$R_E = \sqrt{\frac{4GM}{c^2}\frac{D_S D_{LS}}{D_L}} \tag{21}$$

Here, the mass M, refers to the mass of the stellar mass microlensing inside the lensing galaxy in solar masses. Assuming a mass of 1M$\odot$, R_E=5.038x10^{14}m.

For the system 2M1134-2103 used in this work as discussed in section 1, the quasar observations have been taken for a span of more than a month. The fluctuations detected in one of the images not present in the others can be credited to microlensing if intrinsic variability is ruled out. The microlensing for the system 2M1134-2103 is studied using the MmD technique first introduced in [43] and further developed in [22].

5.1 MmD

The information for this section is explained using [43][22] and [41]. The MmD (macro-micro decomposition) is a technique to detect microlensing in a lensed quasar by linearly combining spectra of a pair of lensed images. The method, as developed in [22] assumes that the observed spectra for an image is a superposition of a spectrum F_M, which is only macrolensed and a spectrum $F_{M\mu}$, which is both micro and macrolensed. F_M and $F_{M\mu}$ can be extracted by using 2 spectra F1 and F2 for different observed lensed images (1 and 2) shown in eqns 22 and 23.

$$F_1 = MF_M + M\mu F_{M\mu}, \tag{22}$$

$$F_2 = F_M + F_{M\mu} \tag{23}$$

M and μ are two multiplicative factors, where M corresponds to the macro-amplication factor and is equal to M1/M2 for images 1 and 2 respectively. μ is the micro amplification factor of the 1st image and thus it is assumed that the 2nd image is not affected by microlensing in a chosen pair.

M can be estimated as the ratio of the 2 spectra, preferably in the narrow line region as, the emission from the narrow line region comes from the most broad part from a region much larger than θ_E and is least likely to be affected by microlensing. F_M and $F_{M\mu}$ can then be written as :

$$F_M = \frac{-A}{A-M}(\frac{F_1}{A} - F_2), \tag{24}$$

$$F_{M\mu} = \frac{M}{A-M}(\frac{F_1}{M} - F_2) \tag{25}$$

where, A=Mμ. If we focus on the decomposition in the vicinity of an emission line, F1 and F2 can be considered as a sum of continuum + an emission profile. So, F_1= F'_c + F'_e and F_2 = F_c + F_e. Thus eqns 24 and 25 can be rewritten as :

$$F_M = \frac{-A}{A-M}(\frac{F'_e}{A} - F_e) \tag{26}$$

$$F_{M\mu} = F_c + \frac{M}{A-M}(\frac{F'_e}{M} - F_e) \tag{27}$$

A is the scaling factor between the continua of F_1 and F_2, so A=F'_c/F_c, and eqns 26 and 27 are used to devise a strategy to derive A and M from the data.

So first, the factor A is measured by making F_M=0 in regions corresponding to continuum emission. A can also be thought of as the mean of the flux ratios of the continuum redward and blueward of an emission line. Afterwards, the ratio M is sought by minimizing the emission above the continuum in $F_{M\mu}$ to obtain a valid decomposition where there is no significant dip or lift in $F_{M\mu}$, thus keeping $F_{M\mu}$ as flat as possible. Finally, with the obtained values of A and M, F_M and $F_{M\mu}$ are scaled according to eqns 24 and 25. The microlensing amplitude, μ is then obtained as μ=A/M.

Both factors M and μ, can have chromatic behaviors. The micro-amplification of the continuum is related to the effective size of the continuum source which can be λ-dependant. For a line profile, μ, can be considered constant but for a different line profile corresponding to different wavelengths, μ can have a different value. Similarly,

M can also vary for different wavelengths due to differential extinction in the lensing galaxy. Another factor to consider is time, at different epochs of observations, M remains identical in absence of intrinsic variability. The amplitude of variation of M can be derived from the quasar's light curve, depending upon the intrinsic variability (how much quasar spectrum varies in amplitude over a period equal to time delay). μ will also vary depending on epochs of observation. If the observational period is long enough, usually several months, depending on the geometry of the system, the lens and the caustics, variations of the microlensing of the continuum or of different parts of BLR can be observed. For the time-frame of the observations taken in the work, which is one month, it may be too small to see a significant change in μ.

MmD decomposition is done for the 4 images of the spectrum, named similar to in [34] as displayed in fig 9. The results are displayed in the following subsections.

5.1.1 Results

The result for the A-B pair around the CIII] blend is shown in fig 32, as observed, microlensing is detected with microlensing amplitude μ=2.42, and also M=0.48 and A=1.16. The values for M, where we observe a valid decomposition are M$\leq$0.48, thus the value of 0.48 is chosen as the maximum value for the magnification factor M. For the cases where microlensing is not detected eg for the B-C pair, then, $\mu \rightarrow 1$ then, M $\rightarrow$ A. In such cases the decomposition is not required and the true spectra are only macro-lensed and A=M.

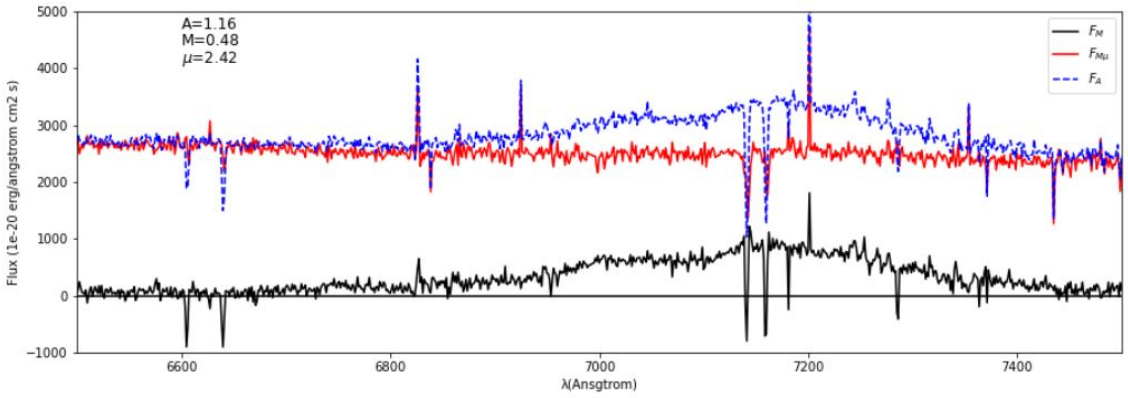

Figure 32: MmD for A-B spectra around CIII] emission

The quality of the decomposition and the errors depend on the S/N ratio of the spectra,

the spectral extraction done in section 3, as well as the strength of the microlensing effect. Other parts of the spectrum can also be visualized to see the microlensing effect and for the A-C pair, this is done around the SiIV+OIV] emission blend as well, shown in fig 33. We can observe that due to the nature of the spectrum here, its harder to derive the amplitude of microlensing in the system, but it is plausible given that we already detect it well for the same pair of spectra around the CIII] blend.

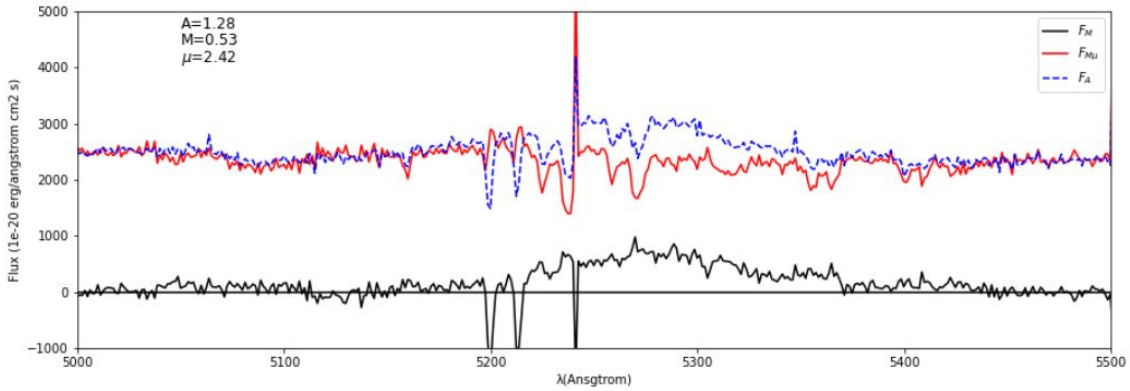

Figure 33: MmD for A-C spectra around SiIV+OIV] emission blend

The results of the decomposition for different pairs of spectra are summarized in table 6.

Spectra pair	**emission region**	μ	**A**	**M**	**microlensing**
A-B	CIII] blend	2.42	1.16	0.48	yes
A-B	SiIV+OIV blend	2.42	1.28	0.53	yes
B-C	CIII] blend	1	1.02	-	no
B-C	SiIV+OIV blend	1	1.12	-	no
C-D	CIII] blend	1	4.8	-	no
C-D	SiIV+OIV blend	1	4.65	-	no
A-C	CIII] blend	2.42	1.16	0.48	yes
A-C	SiIV+OIV blend	2.42	1.2	0.495	yes
B-D	CIII] blend	1	4.82	-	no
B-D	SiIV+OIV blend	1	5.05	-	no
A-D	CIII] blend	2.42	5.6	2.31	yes
A-D	SiIV+OIV blend	2.42	5.9	2.44	yes

Table 6: Results for MmD decomposition for different spectral pairs

From the results, it can clearly be seen that image A is microlensed with a microlensing

amplitude, μ of 2.42. We don't observe any chromatic changes in μ in the different regions of the spectrum but we do observe chromatic changes in M, implying that there is a possibility for differential extinction.

It is clear from fig 32 and fig 33 that the continuum is microlensed, but the BLR is not. Comparing the size of the BLR based on the black hole mass estimation derived in section 4.1, $R_{BLR}/R_E = 1.359$. Since, the sizes are comparable, assuming a $1M\odot$ lens, a deformation of the line would be expected. Similarly, a comparison can be made to compare the size of the continuum region to R_E. In general, its a good approximation that the size of the continuum region is about 10 times smaller than the BLR. Therefore, it is not unexpected to sometimes observe large amplitude microlensing of the continuum.

Another result can be obtained by looking at fig 33, for the SiIV+OIV] blend, the absorption is present in $F_{M\mu}$ for the blend but not for the continuum in F_M and thus this absorption is due to an intrinsic absorber. The absorber could be present exterior to the BLR as the absorption is observed in $F_{M\mu}$ which contains the continuum+BLR flux. This result can be validated by the theory developed in [42], where they observe a similar absorption feature for the MgII line.

Another interesting result from this decomposition is to compare the macro magnification M, with the macro model for this system. The macro magnification based on macro models for HST data for different images of 2M1134-2103 is done in [37]. Adjusting their image labelling conventions to the one taken here, M is summarized in table 7. Comparing table 7 to table 6, we find that the image magnification M obtained in this work agrees with the spectra pair, within uncertainties (which is $\sim$ 10%). For image D, M seems to be slightly overestimated for our data, but using the values of M for spectral pairs involving D from [37], the decomposition still seems to be effective. For all spectra pair involving D, there is a mismatch between the 2 values of M which is a source of systematic uncertainty. The uncertainties here are larger for D ($\sim$ 20%) and can be due to D being the dimmest image in the quasar. The noise in this image is stronger compared to the flux of this image, and since the quality of the extraction and the quality of the decomposition both depend on the noise, the uncertainty is larger.

According to [14], the FeIII emission in the range of 2039-2113 Å which is detected in

Spectra pair	**M(from [37])**	M(from table 6)
A/B	0.523	0.505
B/C	1.055	1.07
C/D	3.88	4.725
A/C	0.552	0.51
B/D	4.09	4.935
A/D	2.14	2.375

Table 7: M obtained in [37]

our spectra in fig 23 could be coming from a region close to the continuum and could be microlensed as well. They use the a virial based technique with the redshift of this emission with respect to the redshift of the quasar and the microlensing detected in this region to calculate the size of this region where the emission originates from and perform an independent estimate of the black hole mass. I performed a MmD decomposition for this line, (fig 34), but unveiled only a weak microlensing. This does not support the result from [14] who claim that this region is systematically microlensed and hence is compact. Since the apparent amplitude of microlensing is weak, and extraction is more uncertain in the reddest part of our spectrum. It could be useful to see has if this result lasts with a more advanced extraction methodology and if so, the emission could result from a compact region.

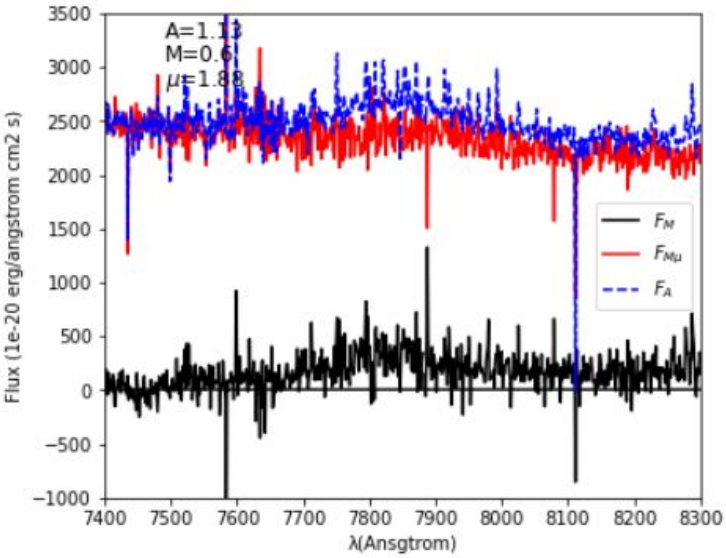

Figure 34: MmD for FeIII (2039-2113) line

6 Conclusion and future prospects

The data reduction process used by the pipeline was deeply investigated in this work and we suggest using default values for most of the parameters and use ZAP for the removal of sky residuals ideally on each exposure. Table 2 is also proposed summarizing the most important parameters that can be changed according to the needs of a future user.

For the system 2M1134-2103, information about the lensing galaxy has not yet been published and so a code was written in the context of this work for spectrum extraction of both the lensing galaxy and the quasar images. The lensing galaxy is identified to be an elliptical galaxy with a redshift of 0.6563 ± 0.00073. Absorptions and emissions are detected in the spectra of both the lensing galaxy and the quasar and the quasar redshift is obtained as 2.77, which is conferred with the results of [34] and [37]. In addition, two of the brightest galaxies nearest (in projection) south-east of the lens were identified, one is an elliptical galaxy with a redshift of 0.239 and the other an irregular galaxy with a redshift of 0.482. Both of these are in the foreground of the lensing galaxy and more work is required to estimate if these galaxies are at the origin of the large shear derived in the models of [34].

The mass for the supermassive black hole at the centre of the quasar system 2M1134 is estimated as $\log(M_{BH}/M\odot) = 8.519 \pm 0.33$. Here, the standard error for the CIV line used to calculate the black hole mass derived in the works of [28] is used to estimate the minimum uncertainty on the derived mass. The uncertainties could be better estimated in a future work as the 0.33 dex here, is a lower bound on the uncertainty neglecting the other sources of uncertainty. Based on the black hole mass, the size of the broad line region is also estimated as $\log(R^{cm}_{BLR}) = 16.8357$.

Microlensing is detected in image A of the system using the MmD technique first introduced in [43]. Image A in fig 9 of the quasar system seems to be microlensed in the epoch of our observational data with a microlensing amplitude $\mu = 2.42$. It is observed from the decomposition, that the continuum is microlensed but the microlensing in the BLR is not detected. It is also found that μ is achromatic over the wavelength range considered.

It is determined if the microlensing in the BLR is plausible by comparing the size of the broad line region (R_{BLR}) and the projected size of the Einstein radius (R_E), their

sizes seem to comparable with a ratio of 1.359, thus making the probability to observe microlensing of the BLR as high. As the continuum is more compact than the BLR, its microlensing is likely. The rather large amplitude of microlensing observed in image A is therefore not surprising. As a future work, it may be interesting to constrain the disc size by comparing the observed amplitude of microlensing in image A to expectation from microlensing probability distribution, derived from a micro-magnification map. Furthermore, constraints on the BLR size could also be derived the same way and compared to the BLR sizes derived from the spectral analysis presented in section 4.1.

During the decomposition, the ratio of macro-magnification M for the images has also been estimated in table 6. It is compared with M for macro-model values obtained by [37] for the system 2M1134-2103 shown in table 7. It seems to be agreeable within uncertainties of 10% for images A, B and C and 20% for image D. M is also observed to be chromatic which could be due to differential extinction in one or two of the images. However, before drawing firm conclusions, a better extraction is required, specially for the redder part of the spectra. Thus the chromaticity of M and achromaticity of μ could be further investigated by performing a better quality extraction of the spectra.

The spectral decomposition method MmD described in section 5.1 is also performed for the FeIII emission between 2039-2113 Å. Microlensing for the emission coupled with its relative redshift could be another way to derive an independent M_{BH} for the system as depicted in the works of [14]. There seems to be weak microlensing of this emission for the system indicating that this emission does not originate from a region as compact as the accretion disk as argued in [14]. Again, a better quality spectrum extraction would be needed to assess this result.

References

[1] Clabon Allen. 'Ch 24 of Allen's Astrophysical Quantities'. In: *Allen's Astrophysical Quantities*. 1955.

[2] NMSU astronomy. *Galaxy Spectra*. Galaxy spectra. URL: http://astronomy.nmsu.edu/nicole/teaching/ASTR505/lectures/lecture26/slide01.html.

[3] Amy J. Barger, ed. *Supermassive Black Holes in the Distant Universe*. Vol. 308. Astrophysics and Space Science Library. Dordrecht: Springer Netherlands, 2004. ISBN: 978-90-481-6662-6 978-1-4020-2471-9. DOI: 10.1007/978-1-4020-2471-9. URL: http://link.springer.com/10.1007/978-1-4020-2471-9.

[4] Volker Beckmann and Chris R. Shrader. *Active Galactic Nuclei*. Publication Title: Active Galactic Nuclei ADS Bibcode: 2012agn..book.....B. 1st Aug. 2012. URL: https://ui.adsabs.harvard.edu/abs/2012agn..book.....B.

[5] R. D. Blandford and C. F. McKee. 'Reverberation mapping of the emission line regions of Seyfert galaxies and quasars'. In: *The Astrophysical Journal* 255 (Apr. 1982), p. 419. ISSN: 0004-637X, 1538-4357. DOI: 10.1086/159843. URL: http://adsabs.harvard.edu/doi/10.1086/159843.

[6] K. Chang and S. Refsdal. 'Flux variations of QSO 0957 + 561 A, B and image splitting by stars near the light path'. In: *Nature* 282.5739 (Dec. 1979), pp. 561–564. ISSN: 0028-0836, 1476-4687. DOI: 10.1038/282561a0. URL: http://www.nature.com/articles/282561a0.

[7] Jean-François Claeskens and Jean Surdej. 'Gravitational lensing in quasar samples'. In: *The Astronomy and Astrophysics Review* 10.4 (Mar. 2002), pp. 263–311. ISSN: 0935-4956, 1432-0754. DOI: 10.1007/s001590000010. URL: http://link.springer.com/10.1007/s001590000010.

[8] The Astropy Collaboration et al. 'The Astropy Project: Building an inclusive, open-science project and status of the v2.0 core package'. In: *The Astronomical Journal* 156.3 (23rd Aug. 2018), p. 123. ISSN: 1538-3881. DOI: 10.3847/1538-3881/aabc4f. arXiv: 1801.02634[astro-ph]. URL: http://arxiv.org/abs/1801.02634.

[9] V. T. Doroshenko et al. 'Broad-line region kinematics and black hole mass in Markarian 6: Black hole mass in Mrk 6'. In: *Monthly Notices of the Royal Astronomical Society* 426.1 (11th Oct. 2012), pp. 416–426. ISSN: 00358711. DOI: 10.1111/j.1365-2966.2012.20843.x. URL: https://academic.oup.com/mnras/article-lookup/doi/10.1111/j.1365-2966.2012.20843.x.

[10] A. S. Eddington. 'The internal constitution of the stars'. In: *The Observatory* 43 (1st Oct. 1920). ADS Bibcode: 1920Obs....43..341E, pp. 341–358. ISSN: 0029-7704. URL: https://ui.adsabs.harvard.edu/abs/1920Obs....43..341E.

[11] A. Einstein. 'Über den Einfluß der Schwerkraft auf die Ausbreitung des Lichtes'. In: *Annalen der Physik* 340.10 (1911), pp. 898–908. ISSN: 00033804, 15213889. DOI: 10.1002/andp.19113401005. URL: https://onlinelibrary.wiley.com/doi/10.1002/andp.19113401005.

[12] Albert Einstein. 'Physics and reality'. In: *Journal of the Franklin Institute* 221.3 (Mar. 1936), pp. 349–382. ISSN: 00160032. DOI: 10.1016/S0016-0032(36)91047-5. URL: https://linkinghub.elsevier.com/retrieve/pii/S0016003236910475.

[13] Andrew C. Fabian. 'Active galactic nuclei'. In: *Proceedings of the National Academy of Sciences* 96.9 (27th Apr. 1999), pp. 4749–4751. ISSN: 0027-8424, 1091-6490. DOI: 10.1073/pnas.96.9.4749. URL: https://pnas.org/doi/full/10.1073/pnas.96.9.4749.

[14] C. Fian et al. 'Revealing the structure of the lensed quasar Q 0957+561: III. SMBH mass via gravitational redshift'. In: *Astronomy & Astrophysics* (26th July 2021). ISSN: 0004-6361, 1432-0746. DOI: 10.1051/0004-6361/202140977. arXiv: 2107.11791[astro-ph]. URL: http://arxiv.org/abs/2107.11791.

[15] W. Freudling et al. 'Automated data reduction workflows for astronomy'. In: *Astronomy & Astrophysics* 559 (Nov. 2013), A96. ISSN: 0004-6361, 1432-0746. DOI: 10.1051/0004-6361/201322494. arXiv: 1311.5411[astro-ph]. URL: http://arxiv.org/abs/1311.5411.

[16] A. Fruchter and et al. *HST MultiDrizzle Handbook*. Publication Title: HST MultiDrizzle ADS Bibcode: 2009hmdi.book.....F. 1st Jan. 2009. URL: https://ui.adsabs.harvard.edu/abs/2009hmdi.book.....F.

[17] J. Gorgas et al. 'Empirical calibration of the 4000 Å break'. In: *Astronomy and Astrophysics Supplement Series* 139.1 (Oct. 1999), pp. 29–41. ISSN: 0365-0138, 1286-4846. DOI: 10.1051/aas:1999375. URL: http://aas.aanda.org/10.1051/aas:1999375.

[18] A. Hamanowicz et al. 'MUSE-ALMA Halos V: Physical properties and environment of z ¡ 1.4 HI quasar absorbers'. In: *Monthly Notices of the Royal Astronomical Society* 492.2 (21st Feb. 2020), pp. 2347–2368. ISSN: 0035-8711, 1365-2966. DOI: 10.1093/mnras/stz3590. arXiv: 1912.08699[astro-ph]. URL: http://arxiv.org/abs/1912.08699.

[19] Jeremy S. Heyl. 'A fast matching algorithm for sheared stellar samples: k-d match'. In: *Monthly Notices of the Royal Astronomical Society* 433.2 (1st Aug. 2013), pp. 935–939. ISSN: 1365-2966, 0035-8711. DOI: 10.1093/mnras/stt781. URL: http://academic.oup.com/mnras/article/433/2/935/1747138/A-fast-matching-algorithm-for-sheared-stellar.

[20] Keith Horne et al. 'Observational Requirements for High-Fidelity Reverberation Mapping'. In: *Publications of the Astronomical Society of the Pacific* 116.819 (May 2004), pp. 465–476. ISSN: 0004-6280, 1538-3873. DOI: 10.1086/420755. URL: http://iopscience.iop.org/article/10.1086/420755.

[21] Tim-Oliver Husser et al. 'MUSE crowded field 3D spectroscopy of over 12 000 stars in the globular cluster NGC 6397: I. The first comprehensive HRD of a globular cluster'. In: *Astronomy & Astrophysics* 588 (Apr. 2016), A148. ISSN: 0004-6361, 1432-0746. DOI: 10.1051/0004-6361/201526949. URL: http://www.aanda.org/10.1051/0004-6361/201526949.

[22] D. Hutsemékers et al. 'Microlensing in H1413+117: disentangling line profile emission and absorption in a broad absorption line quasar'. In: *Astronomy and Astrophysics* 519 (Sept. 2010), A103. ISSN: 0004-6361, 1432-0746. DOI: 10.1051/0004-6361/200913247. URL: http://www.aanda.org/10.1051/0004-6361/200913247.

[23] M. J. Irwin et al. 'Photometric variations in the Q2237 + 0305 system - First detection of a microlensing event'. In: *The Astronomical Journal* 98 (Dec. 1989), p. 1989. ISSN: 00046256. DOI: 10.1086/115272. URL: http://adsabs.harvard.edu/cgi-bin/bib_query?1989AJ.....98.1989I.

[24] S. Kamann, L. Wisotzki and M. M. Roth. 'Resolving stellar populations with crowded field 3D spectroscopy'. In: *Astronomy & Astrophysics* 549 (Jan. 2013), A71. ISSN: 0004-6361, 1432-0746. DOI: 10.1051/0004-6361/201220476. URL: http://www.aanda.org/10.1051/0004-6361/201220476.

[25] Andreas Kelz et al. 'Development and performance of the MUSE calibration unit'. In: SPIE Astronomical Telescopes + Instrumentation. Ed. by Ian S. McLean, Suzanne K. Ramsay and Hideki Takami. Amsterdam, Netherlands, 24th Sept. 2012, 84465T. DOI: 10.1117/12.926003. URL: http://proceedings.spiedigitallibrary.org/proceeding.aspx?doi=10.1117/12.926003.

[26] W. Kollatschny and M. Zetzl. 'The shape of broad-line profiles in active galactic nuclei'. In: *Astronomy & Astrophysics* 549 (Jan. 2013), A100. ISSN: 0004-6361, 1432-0746. DOI: 10.1051/0004-6361/201219411. URL: http://www.aanda.org/10.1051/0004-6361/201219411.

[27] Georges Lemaître. 'Republication of: A homogeneous universe of constant mass and increasing radius accounting for the radial velocity of extra-galactic nebulae'. In: *General Relativity and Gravitation* 45.8 (Aug. 2013), pp. 1635–1646. ISSN: 0001-7701, 1572-9532. DOI: 10.1007/s10714-013-1548-3. URL: http://link.springer.com/10.1007/s10714-013-1548-3.

[28] J. E. Mejía-Restrepo et al. 'Active galactic nuclei at z 1.5 – II. Black hole mass estimation by means of broad emission lines'. In: *Monthly Notices of the Royal Astronomical Society* 460.1 (21st July 2016), pp. 187–211. ISSN: 0035-8711, 1365-2966. DOI: 10.1093/mnras/stw568. URL: https://academic.oup.com/mnras/article-lookup/doi/10.1093/mnras/stw568.

[29] A. F. J. Moffat. 'A Theoretical Investigation of Focal Stellar Images in the Photographic Emulsion and Application to Photographic Photometry'. In: *Astronomy and Astrophysics* 3 (1st Dec. 1969). ADS Bibcode: 1969A&A.....3..455M, p. 455. ISSN: 0004-6361. URL: https://ui.adsabs.harvard.edu/abs/1969A&A.....3..455M.

[30] L. Pasquini et al. 'Installation and commissioning of FLAMES, the VLT Multifibre Facility'. In: *The Messenger* 110 (1st Dec. 2002). ADS Bibcode: 2002Msngr.110....1P, pp. 1–9. ISSN: 0722-6691. URL: https://ui.adsabs.harvard.edu/abs/2002Msngr.110....1P.

[31] B. M. Peterson and K. Horne. 'Reverberation Mapping of Active Galactic Nuclei'. In: *Astronomische Nachrichten* 325.3 (Mar. 2004), pp. 248–251. ISSN: 0004-6337, 1521-3994. DOI: 10.1002/asna.200310207. arXiv: astro-ph/0407538. URL: http://arxiv.org/abs/astro-ph/0407538.

[32] Laure Piqueras et al. *MPDAF - A Python package for the analysis of VLT/MUSE data*. 10th Oct. 2017. arXiv: 1710.03554[astro-ph]. URL: http://arxiv.org/abs/1710.03554.

[33] J. E. Pringle. 'Accretion Discs in Astrophysics'. In: *Annual Review of Astronomy and Astrophysics* 19.1 (Sept. 1981), pp. 137–160. ISSN: 0066-4146, 1545-4282. DOI: 10.1146/annurev.aa.19.090181.001033. URL: https://www.annualreviews.org/doi/10.1146/annurev.aa.19.090181.001033.

[34] Cristian E. Rusu et al. 'A Search for Gravitationally Lensed Quasars and Quasar Pairs in Pan-STARRS1: Spectroscopy and Sources of Shear in the Diamond 2M1134$-$2103'. In: *Monthly Notices of the Royal Astronomical Society* 486.4 (11th July 2019), pp. 4987–5007. ISSN: 0035-8711, 1365-2966. DOI: 10.1093/mnras/stz1142. arXiv: 1803.07175[astro-ph]. URL: http://arxiv.org/abs/1803.07175.

[35] C. Sandin et al. 'P3D: a general data-reduction tool for fiber-fed integral-field spectrographs'. In: *Astronomy and Astrophysics* 515 (June 2010), A35. ISSN: 0004-6361, 1432-0746. DOI: 10.1051/0004-6361/201014022. URL: http://www.aanda.org/10.1051/0004-6361/201014022.

[36] R. W. Schmidt and J. Wambsganss. 'Quasar microlensing'. In: *General Relativity and Gravitation* 42.9 (Sept. 2010), pp. 2127–2150. ISSN: 0001-7701, 1572-9532. DOI: 10.1007/s10714-010-0956-x. URL: http://link.springer.com/10.1007/s10714-010-0956-x.

[37] T. Schmidt et al. *STRIDES: Automated uniform models for 30 quadruply imaged quasars*. 9th June 2022. arXiv: 2206.04696[astro-ph]. URL: http://arxiv.org/abs/2206.04696.

[38] J. Selsing et al. 'An X-Shooter composite of bright 1 ¡ z ¡ 2 quasars from UV to infrared'. In: *Astronomy & Astrophysics* 585 (Jan. 2016), A87. ISSN: 0004-6361, 1432-0746. DOI: 10.1051/0004-6361/201527096. URL: http://www.aanda.org/10.1051/0004-6361/201527096.

[39] Yue Shen. *The Mass of Quasars*. 11th Feb. 2013. arXiv: 1302.2643[astro-ph]. URL: http://arxiv.org/abs/1302.2643.

[40] J. L. Simon et al. 'Numerical expressions for precession formulae and mean elements for the Moon and the planets.' In: *Astronomy and Astrophysics* 282 (1st Feb. 1994). ADS Bibcode: 1994A&A...282..663S, p. 663. ISSN: 0004-6361. URL: https://ui.adsabs.harvard.edu/abs/1994A&A...282..663S.

[41] D. Sluse et al. 'Microlensing of the broad line region in 17 lensed quasars'. In: *Astronomy & Astrophysics* 544 (Aug. 2012), A62. ISSN: 0004-6361, 1432-0746. DOI: 10.1051/0004-6361/201219125. arXiv: 1206.0731[astro-ph]. URL: http://arxiv.org/abs/1206.0731.

[42] D. Sluse et al. *Microlensing probes the AGN structure of the lensed quasar J1131-1231*. 17th Jan. 2008. arXiv: 0801.2698[astro-ph]. URL: http://arxiv.org/abs/0801.2698.

[43] D. Sluse et al. 'Multi-wavelength study of the gravitational lens system RXS J1131-1231: III. Long slit spectroscopy: micro-lensing probes the QSO structure'. In: *Astronomy & Astrophysics* 468.3 (June 2007), pp. 885–901. ISSN: 0004-6361, 1432-0746. DOI: 10.1051/0004-6361:20066821. URL: http://www.aanda.org/10.1051/0004-6361:20066821.

[44] Kurt T. Soto et al. 'ZAP – Enhanced PCA Sky Subtraction for Integral Field Spectroscopy'. In: (2016). Publisher: arXiv Version Number: 1. DOI: 10.48550/ARXIV.1602.08037. URL: https://arxiv.org/abs/1602.08037.

[45] Peter B. Stetson. 'DAOPHOT - A computer program for crowded-field stellar photometry'. In: *Publications of the Astronomical Society of the Pacific* 99 (Mar. 1987), p. 191. ISSN: 0004-6280, 1538-3873. DOI: 10.1086/131977. URL: http://iopscience.iop.org/article/10.1086/131977.

[46] MUSE Pipeline Team. 'MUSE Pipeline User Manual'. In: (27th Apr. 2021), p. 156.

[47] Harvard University. *XCSAO Templates used at the Center for Astrophysics*. URL: http://tdc-www.harvard.edu/software/rvsao/Templates/.

[48] Peter M. Weilbacher et al. 'The data processing pipeline for the MUSE instrument'. In: *Astronomy & Astrophysics* 641 (Sept. 2020), A28. ISSN: 0004-6361, 1432-0746. DOI: 10.1051/0004-6361/202037855. URL: https://www.aanda.org/10.1051/0004-6361/202037855.

[49] Jong-Hak Woo et al. 'THE BLACK HOLE MASS–STELLAR VELOCITY DISPERSION RELATION OF NARROW-LINE SEYFERT 1 GALAXIES'. In: *The Astrophysical Journal* 801.1 (27th Feb. 2015), p. 38. ISSN: 1538-4357. DOI: 10.1088/0004-637X/801/1/38. URL: https://iopscience.iop.org/article/10.1088/0004-637X/801/1/38.

[50] E. L. Wright. 'A Cosmology Calculator for the World Wide Web'. In: *Publications of the Astronomical Society of the Pacific* 118.850 (Dec. 2006), pp. 1711–1715. ISSN: 0004-6280, 1538-3873. DOI: 10.1086/510102. URL: http://iopscience.iop.org/article/10.1086/510102.